IEEE Access
Multidisciplinary ⋮ Rapid Review ⋮ Open Access Journal

Received April 13, 2021, accepted April 29, 2021, date of publication May 6, 2021, date of current version May 13, 2021.

Digital Object Identifier 10.1109/ACCESS.2021.3078078

Grid-Forming Converters Control Based on the Reactive Power Synchronization Method for Renewable Power Plants

JOSÉ LUIS RODRÍGUEZ AMENEDO, (Senior Member, IEEE), SANTIAGO ARNALTES GÓMEZ, JAIME ALONSO-MARTINEZ, AND MARCIAL GONZÁLEZ DE ARMAS

Department of Electrical Engineering, University Carlos III of Madrid, 28911 Leganés, Spain

Corresponding author: José Luis Rodríguez Amenedo (amenedo@ing.uc3m.es)

This work was supported by the Autonomous Community of Madrid through the PROMINT-CM under Project S2018/EMT-4366.

ABSTRACT The massive penetration of renewable energy sources in electrical systems has been displacing synchronous generators (SGs) from conventional power plants in the last few years. Renewable generation plants are usually connected to power grids through electronic power converters, which cannot provide the same power generation services as SGs due to their mode of operation. Recently, different concepts have been proposed for electronic converter control in an attempt to emulate the performance of SGs, resulting in the so-called grid-forming converters (GFCs). This paper proposes a new GFC control strategy based on the reactive power synchronization (RPS) method, which decouples the synchronizing power and the active power control of renewable generation source to which a converter is connected. For this purpose, this study assesses three power sources: batteries, photovoltaic (PV) plants, and full-converter wind turbines. Moreover, the study proposes models and controls for each of these sources, whose dynamics exert a decisive influence on the grid services provided by renewable energy plants. Thereafter, the study proposes a GFC–RPS control scheme and verifies its effectiveness in different applications; for example, inertial response, which provides power immediately through a fast frequency response after a grid has experienced a load variation. Unlike storage systems and wind turbines, PV plants can only render these services if they are not operating at maximum power. Further, the study validates the GFC–RPS control strategy for regulating AC voltage at the output terminals of a converter. Finally, the paper assesses GFC hot swapping during the transition from a grid-connected to an isolated-operation mode while feeding a dynamic load. Results revealed that both the voltage and frequency remain stable, thereby demonstrating that the proposed GFC–RPS control indeed acts as a true voltage source and emulates the behavior of a conventional SG.

INDEX TERMS Grid-forming power converter, renewable energy sources, reactive power synchronization, fast frequency response, converter hot swapping.

I. INTRODUCTION

The concept of grid-forming converters (GFCs) was first introduced within the context of microgrids [1], [2] as a novel control method for voltage source converters (VSCs) acting as uninterruptible power supplies aimed at maintaining voltage and frequency at the load when it becomes disconnected from microgrids. GFCs act as voltage sources with low-series impedance, which implies that synchronization systems must be accurate enough to support parallel operations with other GFCs supplying isolated loads.

The associate editor coordinating the review of this manuscript and approving it for publication was Youngjin Kim.

However, in recent years, GFC development has risen to a greater dimension due to the massive integration of renewable energy sources in power systems. Renewable energy systems are usually connected to a grid through electronic power converters, which are increasingly displacing synchronous generators (SGs) used in conventional power plants. These SGs traditionally control the voltage and frequency of power grids. Current energy generation scenarios in many European electricity systems reveal that at certain periods of time, an extremely high percentage of energy demand (>70%) is covered by renewable generation, and some countries are even proposing renewable generation to meet 100% of the total energy demand in the forthcoming decades [3].

From a grid standpoint, converters operating in grid-following mode are considered voltage-controlled current sources, as opposed to SGs, which act as voltage sources. International grid codes [4] set forth operating criteria for renewable generation in terms of the following grid services: a) power/frequency control, b) reactive/voltage control, and c) supply continuity in the events of voltage dips (e.g., fault ride through). The problem with grid-following converters is that their services are always provided once voltage and frequency are measured at their terminals, which is known as grid supporting. For example, a power–frequency (P/f) regulation service is executed using a phase-locked loop (PLL) to measure frequency deviations to increase or decrease active power. This method emulates the operation of SG governors. However, some studies suggest that they can produce grid instability when emulating the inertial response of these generators at extremely high electronic converter penetration rates [4], [5].

Frequency deviation is the result of an imbalance between generated and consumed active power in an electrical system. Grid-following converters always render services in a delayed manner after a power imbalance effect has occurred as they measure the imbalance through frequency and act accordingly. In a synchronous generation scenario, converters working in this mode will maintain frequency initially, but they will not be able to completely control it by themselves. Therefore, renewable generation plants are not normally allowed to feed local loads isolated from a grid and must include ''anti-islanding'' protection [6].

Furthermore, GFCs commonly emulate SG behavior. In these instances, the control system's orientation angle (θ) that is determined by measuring voltage directly at converter terminals through a PLL, it is now replaced by the integral action of the frequency deviation, $\Delta\omega$, which it is calculated through an active power synchronization loop, or through reactive power as the current study proposes. In recent years, several research studies have been published on GFC grid synchronization methods, but most of them have focused on active power synchronization loops [7]–[11]. References [7]–[9] discuss the design of active power synchronization methods against disturbance rejection, voltage harmonics, unbalance, phase jump, and frequency deviation events. Furthermore, [10], [11] study the stability of synchronization processes in weak grids and during voltage dips. The simplest synchronization method comprises a droop regulator that determines frequency increase, $\Delta\omega$, based on active power deviation from an established reference value [12]–[14]. Although this method has been widely used in microgrid applications, the first synchronization scheme for VSC converters connected to a grid without a specific synchronization unit was introduced by Zhang *et al.* in [15]. This synchronization process was initially proposed for high-voltage direct current (HVDC) converters, but it has finally been extended to other applications. This technique uses controls to emulate synchronizing torque naturally offered by SGs. This led some researchers to propose the use of controlled-operated power synchronization loops to reproduce the oscillation equation of an SG. These controls are known as a virtual synchronous machine (VSM), [14], [16], [17]. A synchronverter is based on a similar approach [18], but it emulates SGs without using any specific synchronization unit. Finally, [19] presents a synchronous power converter (SPC), whose operating principle is based on determining frequency deviation, $\Delta\omega$, from a second-order function applied to the variation between the measured and reference active powers. This technique uses an additional frequency loop to modify the active power reference when a deviation exists between the reference frequency and frequency recorded by a PLL.

All the aforementioned techniques use an active power synchronization (APS) loop; however, a similar technique also exists based on reactive power synchronization (RPS) [20]–[24]. This technique is grounded on the relationship between the active and reactive powers exchanged instantaneously by the GFC as per the dynamic equations of the interconnection grid. GFC–RPS was first proposed in [20] as a frequency control scheme for the internal grid of offshore wind farms connected to HVDC links through LCC rectifiers. Uncontrolled rectifiers (including units with diode rectifiers) can be used in offshore wind farms because their power flows in a single direction. These rectifiers are also more affordable and robust compared to HVDC-VSC rectifiers, but they need a stable AC grid to switch. This work proposes a central solution wherein a GFC is connected to the input terminals at a rectifier station, and it is supported by a capacitor bank. Later, [22] discussed the possibility of implementing controls without capacitors. In [21], the authors applied the same control technique, but in a distributed manner. Here, the front-end converters of full-converter (FC) wind turbines maintain the frequency of internal AC grid and simultaneously achieve an equitable distribution of the reactive power generated by a wind turbine farm. In [23], the authors assessed the dynamic relationship between active and reactive powers, as well as the control strategies used to synchronize converters to a grid by measuring reactive power. The advantage of this proposal is that the active power channel remains free, without the synchronization loop being affected by the dynamics of the renewable energy source. Moreover, [24] proposes an extension of the RPS concept but applied to controlling the distributed frequency of FC wind generators in black-start applications.

Another important aspect regarding the operation of GFCs is the transition between the grid-connected operation and isolated modes, or vice versa, which is known as hot swapping. However, this transition implies a significant disturbance of voltage and frequency [50]–[52].

Most of the control proposals discussed in previous studies assume an ideal DC voltage source in the DC link capable of providing all the energy demanded by the AC terminals. However, in wind generators and photovoltaic plants, GFC responses actually depend on the dynamics of the source. The present paper specifically addresses GFC control strategies

using RPS applied to renewable generation sources (wind generators, photovoltaic plants, and batteries). Moreover, it assesses and discusses their response to frequency variations, AC voltage controls, and during the transition between the grid-connection and isolated modes of operation.

This paper is organized as follows: Section II provides a system overview, and Section III discusses basic RPS principles applied to a simple grid comprising a GFC connected to a voltage source with an impedance Z_g and modeled by its dynamic equations. Section III also proposes a linear model in the state space and obtains transfer functions for active and reactive power increments in terms of voltage and angle module variations. Thereafter, Section IV presents the RPS control scheme, as well as a block diagram for the plant model and RPS controls. Likewise, a resulting oscillation equation is calculated as a second-order function that establishes a relationship between angle and active power variations, similar to an SG. Section V discusses renewable generation plant models for sources connected to a converter, as well as active power regulation schemes. Further, Section VI examines regulator designs, and Section VII provides the results from the simulations conducted for each of the technologies analyzed. Specifically, Section VII addresses GFC responses against grid load variations, AC voltage controls, and the transition process between grid-connected and isolated modes, feeding a dynamic load on converter terminals when a circuit breaker trip occurs. Finally, Section VIII discusses our conclusions from this study.

II. SYSTEM DESCRIPTION

Fig. 1 illustrates a system scheme composed by a grid-forming controlled voltage source electronic converter connected to a grid. The voltage across the DC bus terminals is V_{dc}, and the input current is I_{dc}. The converter is connected to the point of common coupling (PCC) through an LC filter. The GFC is controlled by measuring the current, i, PCC voltage, V, and grid current, i_g. The instantaneous active power, P_g, and reactive power, Q_g, values are calculated at the point where the GFC is interconnected with the grid.

A breaker is then connected between the PCC terminals and the grid, and its state determines the operation mode of the GFC (on: grid connected, off: islanded). The grid is modeled through a Thévenin equivalent formed by a voltage source with an amplitude of V_g, a frequency of ω_g, short-circuit impedance of Z_g, and ratio of X/R.

In fact, different renewable generation sources can be connected to DC VSC terminals. Fig. 2 denotes the three different DC sources assessed in this work. The left panel (Fig. 2a) displays a battery. The central panel (Fig. 2b) displays a variable-speed type-IV (full converter) wind generator comprising a wind turbine coupled to an electric generator controlled through a back-end converter. Finally, the right panel (Fig. 2c) represents a photovoltaic (PV) generator. The current generated by the battery is expressed as I_{bat}, DC current from the full converter is expressed as I_{fc}, and current from the PV generator is expressed as I_{pv}.

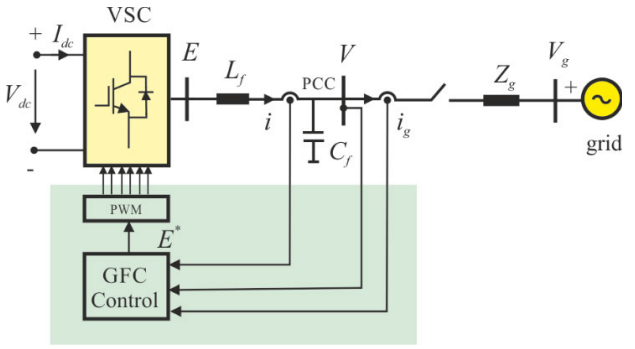

FIGURE 1. System description of a three-phase grid-forming voltage source converter connected to the grid.

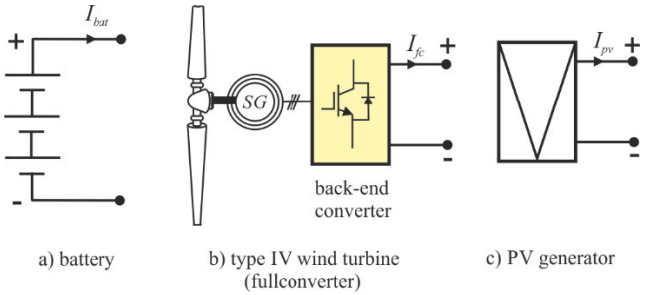

FIGURE 2. DC sources: a) battery, b) wind turbine, c) PV generator.

III. REACTIVE POWER SYNCHRONIZATION

To assess the existing relationship between the instantaneous active and reactive powers generated by the GFC against an increase in voltage and angle, the model illustrated in Fig. 3 is used. In this figure, the GFC is represented as a voltage source behind an impedance connected to a grid with frequency, ω_0. The grid voltage is taken as a phase reference of $\overline{V}_g = V_g\angle 0$, where grid impedance is represented by $\overline{Z}_g = R_g + j\omega_0 L_g$. The GFC voltage is $\overline{V} = V\angle\delta$, and the angle, δ, represents the angular difference between the two voltages.

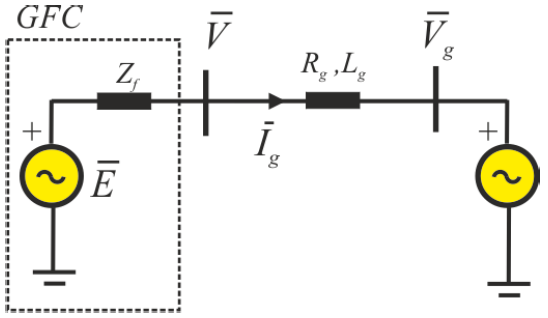

FIGURE 3. Simplified representation of a GFC connected to a grid.

Complex power, $\overline{S}_g = P_g + jQ_g$, is calculated in steady state based on PCC output as

$$\overline{S}_g = P_g + jQ_g = \overline{V}\left(\frac{\overline{V} - \overline{V}_g}{\overline{Z}_g}\right)^* \quad (1)$$

where all the magnitudes are expressed per unit (pu). The term in parentheses represents the current phasor, $\bar{I}_g$, and the symbol $(*)$ indicates the corresponding complex conjugate.

Fig. 4 displays the vector diagram of the voltage and current phasors.

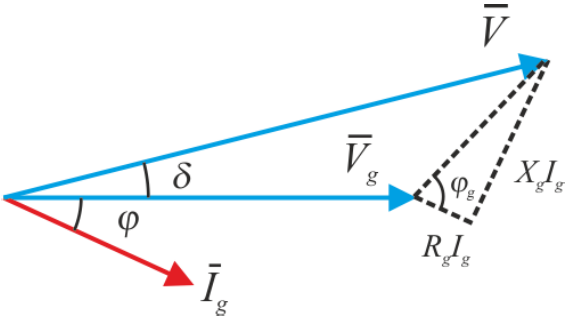

FIGURE 4. Voltages and current vector diagram.

Considering $\bar{Z}_g = Z_g e^{j\varphi_g}$ and separating the real and imaginary parts, the active and reactive powers can be expressed as follows:

$$P_g = \frac{V}{Z_g}\left(V cos\varphi_g - V_g cos(\varphi_g + \delta)\right)$$
$$Q_g = \frac{V}{Z_g}\left(V sin\varphi_g - V_g sin(\varphi_g + \delta)\right). \quad (2)$$

If $R_g = 0$, then

$$P_g = \frac{VV_g}{X_g} sin\delta \quad Q_g = \left(\frac{V}{X_g}\right)\left(V - V_g cos\delta\right). \quad (3)$$

The dynamic equations for the circuit illustrated in Fig. 3 expressed in per unit for a dq reference frame rotating at a speed of ω_0 are

$$\bar{V} - \bar{V}_g = R_g \bar{I}_g + \frac{L_g}{\omega_0}\frac{d\bar{I}_g}{dt} + jL_g\bar{I}_g \quad (4)$$

where $\bar{V} = v_d + jv_q$, $\bar{V}_g = v_{dg} + jv_{qg}$, and $\bar{I}_g = i_{dg} + ji_{qg}$.

When considering voltage, $\bar{V}_g$, as a reference, the v_{qg} component is zero, and the voltages $v_d = V cos\delta$ and $v_q = V sin\delta$. Taking the real and imaginary parts in (4), we obtain the following dynamic equations:

$$V cos\delta - V_g = R_g i_{dg} + \frac{L_g}{\omega_0}\frac{di_{dg}}{dt} - L_g i_{qg}$$
$$V sin\delta = R_g i_{qg} + \frac{L_g}{\omega_0}\frac{di_{qg}}{dt} + L_g i_{dg}. \quad (5)$$

The state variables of this system are i_{dg} and i_{qg}, and the inputs are V, V_g, and δ, where the values of the active and reactive powers are

$$P_g = v_d i_{dg} + v_q i_{qg} = (V cos\delta)\, i_{dg} + (V sin\delta)\, i_{qg}$$
$$Q_g = v_q i_{dg} - v_d i_{qg} = (V sin\delta)\, i_{dg} - (V cos\delta)\, i_{qg}. \quad (6)$$

Next, the variations of the instantaneous active and reactive powers transmitted by the GFC after an angle step of δ and a voltage step of V are obtained. The grid parameter values are as follows: $R_g = 0.01$ pu and $L_g = 0.15$ pu ($Z_g = 0.1503$ pu and $\varphi_g = 86.19°$) at a frequency of 50 Hz ($\omega_0 = 100\pi$ rad/s).

A. VOLTAGE ANGLE STEP

Fig. 5 denotes the transient variation of P_g and Q_g at t = 0.1 s, when a step of $\delta = 8.62°$ is generated against the grid voltage. Here, the GFC and grid voltage magnitude both remain constant at $V = V_g = 1$ pu.

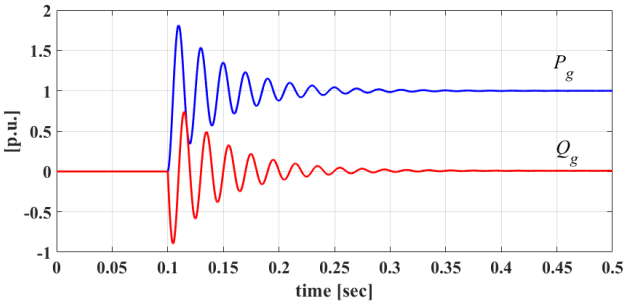

FIGURE 5. Active and reactive power response to a step in the GFC voltage angle.

As can observed, the active power increases until matching its steady-state value of $P_g = 1$ pu through damped oscillation. Reactive power also oscillates until it reaches its steady-state value of $Q_g = 0.09$ pu. Both powers converge to their steady-state values, but during their transient state, power oscillations are similar in amplitude although they pulse in counter phase.

Fig. 6 displays the power values recorded in a PQ plot. This figure clearly denotes the damped oscillation of both powers describing a spiral starting from the (0,0) point and converging on the final steady-state point at (1, 0.089). The spiral is traversed from left to right in such a way that, as the active power increases, the reactive power decreases.

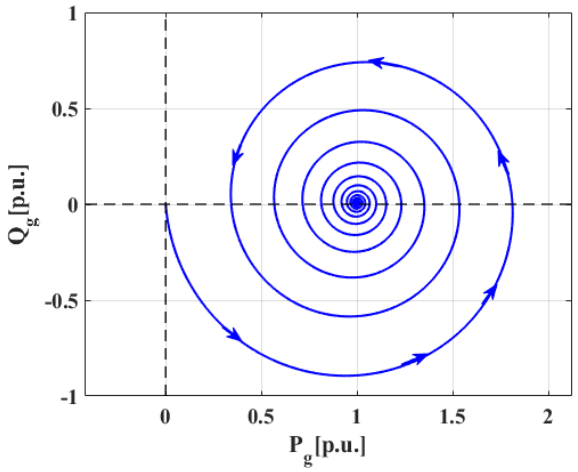

FIGURE 6. PQ plot. Step in the GFC voltage angle.

B. VOLTAGE AMPLITUDE STEP

The same analysis is conducted when the magnitude of the GFC voltage changes from $V = 1$ to 1.075 pu. The voltage angle at the PCC is held constant and equal to $\delta = 0°$. Fig. 7 denotes the transient variation of the active

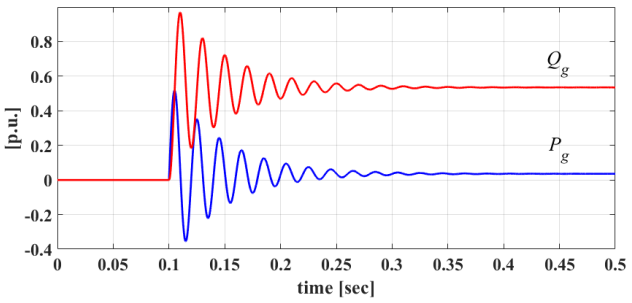

FIGURE 7. Active and reactive power response to a step in the GFC voltage amplitude.

and reactive powers. Both the powers oscillate in phases, but the active power remains approximately constant, and the reactive power increases until it reaches its steady-state value at $Q_g = 0.5$ pu.

The powers in the PQ plane also describe a spiral from the (0,0) point to (0.02,0.5) pu. In this case, both the powers oscillate in phases, i.e., a positive change in the active power causes a positive change in the reactive power, and vice versa. Fig. 8 illustrates the evolution of the P_g and Q_g powers in the PQ plane against changes in PCC voltage amplitude.

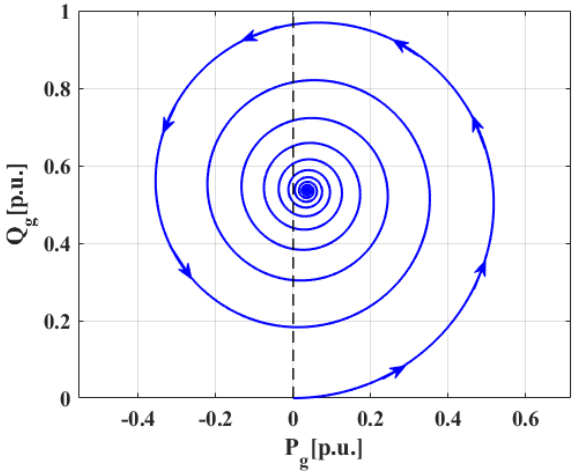

FIGURE 8. PQ plot. Step in the GFC voltage amplitude.

C. STATE-SPACE LINEAR MODEL

By linearizing the dynamic equations from (5) at a given operation point, the following linear model is obtained in the state space:

$$\begin{bmatrix} \frac{d\Delta i_{dg}}{dt} \\ \frac{d\Delta i_{qg}}{dt} \end{bmatrix} = A \begin{bmatrix} \Delta i_{dg} \\ \Delta i_{qg} \end{bmatrix} + B \begin{bmatrix} \Delta V \\ \Delta \delta \end{bmatrix}$$
$$\begin{bmatrix} \Delta P_g \\ \Delta Q_g \end{bmatrix} = C \begin{bmatrix} \Delta i_{dg} \\ \Delta i_{qg} \end{bmatrix} + D \begin{bmatrix} \Delta V \\ \Delta \delta \end{bmatrix} \tag{7}$$

where the state variable vector is $[\boldsymbol{x}] = [\Delta i_{dg}, \Delta i_{qg}]^t$, input vector is $[\boldsymbol{u}] = [\Delta V, \Delta\delta]^t$, and output vector is $[\boldsymbol{y}] = [\Delta P_g, \Delta Q_g]^t$.

The state matrix, A, is equal to

$$A = \omega_0 \begin{bmatrix} -\frac{R_g}{L_g} & +1 \\ -1 & -\frac{R_g}{L_g} \end{bmatrix}. \tag{8}$$

The parameters of the state matrix are expressed in pu, and the matrix items in (8) are expressed in rad/s because the matrix is multiplied by the base frequency, ω_0. As the matrix eigenvalues are calculated from $|\lambda I - A| = 0$, then

$$\left(\lambda + \frac{R_g}{L_g}\omega_0\right)^2 + \omega_0^2 = 0, \tag{9}$$

whose solution is

$$\lambda_{1,2} = -\xi\omega_n \pm j\omega_n\sqrt{1-\xi^2} \tag{10}$$

where ξ is the damping coefficient, and ω_n is the natural frequency, whose expressions in terms of the plant parameters are

$$\omega_n = \omega_0\sqrt{1+\left(\frac{R_g}{L_g}\right)^2}$$
$$\xi = \left(\frac{\omega_0}{\omega_n}\right)\left(\frac{R_g}{L_g}\right). \tag{11}$$

The values from (11) for the $R_g = 0.01$ pu, $L_g = 0.15$ pu, and $\omega_0 = 100\pi$ rad/s plant parameters are as follows: $\omega_n = 314.86$ rad/s and $\xi = 0.07$ pu. Substituting the expressions from (10) into (9), the $\lambda_{1,2}$ eigenvalues are expressed as

$$\lambda_{1,2} = -\frac{R_g}{L_g}\omega_0 \pm j\omega_0 \tag{12}$$

where $\lambda_{1,2} = -20.94 \pm j314.16$ rad/s for the values above. The expressions for the B, C, and D matrices are available in Appendix A hereto.

From the linear model matrices, the transfer functions between the outputs $(\Delta P_g, \Delta Q_g)$ and inputs $(\Delta V, \Delta\delta)$ can be calculated as per the following matrix:

$$C\,(sI - A)^{-1}\,B = \begin{bmatrix} \left(\frac{\Delta P_g}{\Delta V}\right) & \left(\frac{\Delta P_g}{\Delta \delta}\right) \\ \left(\frac{\Delta Q_g}{\Delta V}\right) & \left(\frac{\Delta Q_g}{\Delta \delta}\right) \end{bmatrix} \tag{13}$$

where $s = j\omega$.

Developing the matrix expression from (13), the transfer functions corresponding to the main diagonal are obtained:

$$\left(\frac{\Delta P_g}{\Delta V}\right) = -\frac{1}{V_0}\left(\frac{\Delta Q_g}{\Delta \delta}\right) = \frac{V_0\left(s + \frac{R_g}{L_g}\omega_0\right)}{\left(s + \frac{R_g}{L_g}\omega_0\right)^2 + \omega_0^2}. \tag{14}$$

Likewise, the secondary diagonal for the other two functions are also obtained:

$$\left(\frac{\Delta Q_g}{\Delta V}\right) = +\frac{1}{V_0}\left(\frac{\Delta P_g}{\Delta \delta}\right) = \frac{V_0\omega_0}{\left(s + \frac{R_g}{L_g}\omega_0\right)^2 + \omega_0^2}. \tag{15}$$

Dividing equations (14) and (15), the active and reactive power variation ratio against an angle increase are obtained:

$$\left(\frac{\Delta P_g}{\Delta\delta}\right) = -\frac{\omega_0}{\left(s + \frac{R_g}{L_g}\omega_0\right)}\left(\frac{\Delta Q_g}{\Delta\delta}\right). \tag{16}$$

For voltage variations, the expression is equal to (16) but interchanging the positions of P_g and Q_g, as well as the sign of the equation:

$$\left(\frac{\Delta Q_g}{\Delta V}\right) = +\frac{\omega_0}{\left(s + \frac{R_g}{L_g}\omega_0\right)}\left(\frac{\Delta P_g}{\Delta V}\right). \tag{17}$$

Expressions (16) and (17) are consistent with the results presented in Fig. 5 and Fig. 7. When a change in the GFC voltage angle of $\Delta\delta = 8.62^{\circ}$ is applied, the active power, P_g, reaches its rated power after a damped oscillation. In this case, the reactive power, Q_g, oscillates in the opposite direction, but remains practically zero. The same reasoning is valid for active and reactive power variations against a GFC voltage change. When $\Delta V = 0.075$ pu, the active and reactive power variations produce damped oscillations in the same direction, but the reactive power stabilizes at a value of $Q_g = 0.5$ pu and active power at a value of $P_g = 0.03$ pu. Also considering, R = 0, the relationship is expressed as the derivative of the function.

Next, the transfer function of the reactive power change, ΔQ_g, in terms of the normalized frequency, $\Delta\omega$, is calculated as follows:

$$\left(\frac{\Delta Q_g}{\Delta\omega}\right) = \left(\frac{\Delta Q_g}{\Delta\delta}\right)\left(\frac{\Delta\delta}{\Delta\omega}\right) = \left(\frac{\Delta Q_g}{\Delta\delta}\right)\frac{\omega_0}{s} \tag{18}$$

where $\Delta\delta/\Delta\omega = \omega_0/s$.

Solving $(\Delta Q_g/\Delta\delta)$ in (16) and replacing it in (18), then

$$\left(\frac{\Delta Q_g}{\Delta\omega}\right) = -\frac{\left(s + \frac{R_g}{L_g}\omega_0\right)}{\omega_0}\left(\frac{\omega_0}{s}\right)\left(\frac{\Delta P_g}{\Delta\delta}\right). \tag{19}$$

At $R_g = 0$, the pole-zero pair from the previous equation is cancelled out, and the transfer function for the reactive power with respect to the frequency is equal to the active power variation with respect to the angle:

$$\left(\frac{\Delta Q_g}{\Delta\omega}\right) = -\left(\frac{\Delta P_g}{\Delta\delta}\right). \tag{20}$$

This equation indicates that, at constant voltage, the reactive power is the derivative of P_g with respect to the angle, δ, as can observed in (6).

This conclusion demonstrates the possibility of synchronizing through the RPS method, where, if the active power of the grid, ΔP_g, changes due to an angle change of $\Delta\delta$, the instantaneous reactive power also changes. Against an instantaneous change in ΔQ_g, $\Delta\omega$ is calculated using a droop, which allows to calculate the angular reference, δ, of the converter by integration. The following section discusses the GFC control scheme based on RPS.

IV. GRID-FORMING CONVERTER CONTROL

Fig. 9 denotes the general scheme for the GFC control system based on reactive power synchronization represented by the RPS block. To perform this control, the instantaneous currents of the three-phase grid represented by the $[\boldsymbol{i}]_{g,abc}$ and the current at the output of the converter, $[\boldsymbol{i}]_{abc}$ are measured. Likewise, the instantaneous PCC voltages are measured $[\boldsymbol{v}]_{abc}$.

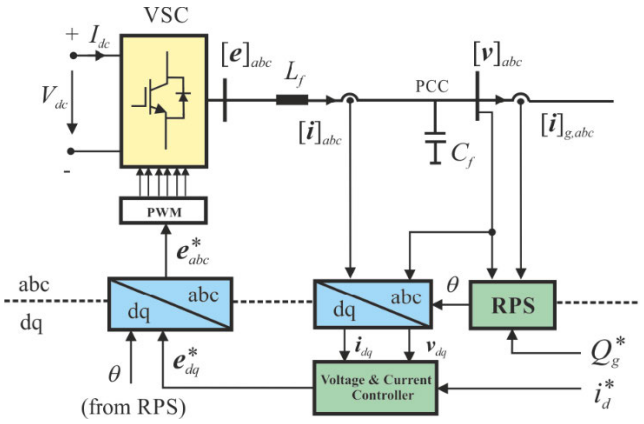

FIGURE 9. General scheme of the GFC control.

This control obtains the angle, θ, through the RPS block, which positions the d axis in a dq rotary axes system with respect to a stationary reference axis, α (Fig. 10). The angle, θ, is then used to determine the dq components of the current at the output of the converter $\boldsymbol{i}_{dq} = i_d + ji_q$, as well as the PPC dq voltages $\boldsymbol{v}_{dq} = v_d + jv_q$, through a Park transformation (abc/dq). The voltage and current controllers use these variables as input to align the PCC voltage vector toward the d axis of the rotary system ($v_q = 0$) and to control the reference current, i^*_d, which is associated with the active power generated when the $\boldsymbol{v}_{dq}$ voltage vector is oriented toward the d axis.

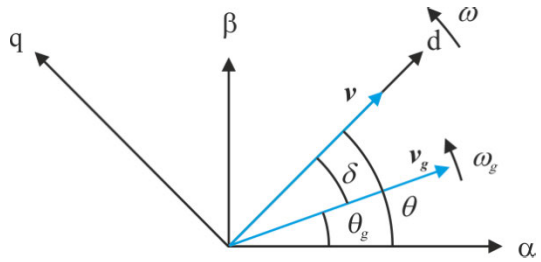

FIGURE 10. Voltage vector diagram.

Fig. 10 denotes the vector diagram for the PCC, $\boldsymbol{v}$, and grid, $\boldsymbol{v_g}$, voltages. As mentioned earlier, the $\boldsymbol{v}$ voltage vector remains controlled-aligned to the d axis, rotating at a speed of ω, and its angular position with respect to the reference axis is θ. In turn, the $\boldsymbol{v_g}$ vector rotates at a speed of ω_g, forming an angle of θ_g. The angle, δ, represents the angular difference between both vectors and remains constant when $\omega = \omega_g$. According to (3), the active power transmitted from the

GFC to grid in steady state is proportional to $sin\delta$. The dynamics of the power angle, δ, are determined by the following expression:

$$\frac{1}{\omega_0}\frac{d\delta}{dt} = \overline{\omega} - \overline{\omega}_g \tag{21}$$

where $\overline{\omega}$ and $\overline{\omega}_g$ represent the control system and grid frequencies, respectively, expressed in pu.

A. REACTIVE POWER SYNCHRONIZATION BLOCK

As discussed in Section III, a dynamic relationship exists between the reactive power, Q_g, and power angle, δ, when the GFC transfers the active power, P_g, to the grid. This relationship will be used as a synchronization mechanism.

Fig. 11 denotes the reactive power synchronization loop corresponding to the RPS block. The difference between the reference reactive power, Q_g^*, and reactive power measured at the GFC output, Q_g, determines the per unit frequency increase, $\Delta\overline{\omega}$, that must be applied to the control to obtain an angle of θ through the synchronization constant, K_s.

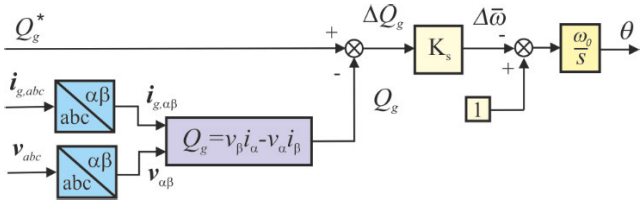

FIGURE 11. Reactive power synchronization loop.

The reactive power calculation is performed based on the output of the GFC expressed in normalized values using a Clarke transformation for the $[\boldsymbol{i}]_{g,abc}$ and $[\boldsymbol{v}]_{abc}$ instantaneous values. When the grid is synchronized at a frequency of ω_0, then $\Delta\overline{\omega} = 0$, and the generated reactive power matches the reference power as $Q_g^* = Q_g$. If the grid frequency is different from ω_0, then $Q_g^* \neq Q_g$ to compensate for frequency deviation through the synchronization loop. If the main breaker trips, the currents of the $[\boldsymbol{i}]_{g,abc}$ vector become null, and the GFC enters in an islanded mode. In this condition of $\Delta Q_g = 0$, the feeding frequency of a load connected to the GFC terminals would be ω_0.

Here, the RPS block does not act as a PLL following the existing PCC voltage angle. Instead, it establishes a synchronization component by modifying the internal frequency increase, $\Delta\overline{\omega}$, after measuring the reactive power. As it will discussed in the following sections, the GFC can operate in islanded mode after the tripping of the main breaker by controlling PCC voltage amplitude and frequency values. However, this will not happen if the converter is operating in a grid-following mode. When the breaker trips, the PLL measures the generated voltage angle, without a suitable control reference.

B. VOLTAGE AND CURRENT CONTROLLER

The GFC controller, as illustrated in Fig. 9, receives the dq values from the $[\boldsymbol{i}]_{abc}$ currents and $[\boldsymbol{v}]_{abc}$ voltages after the Park transformation is conducted using the angle, θ, obtained from the RPS block. This controller has an inner current control loop for the dq components and an outer voltage control loop, which keeps the voltage vector aligned to the d axis from the reference rotary system, implying that $v_q = 0$. Fig. 12 illustrates a block diagram for the dq current and voltage controller.

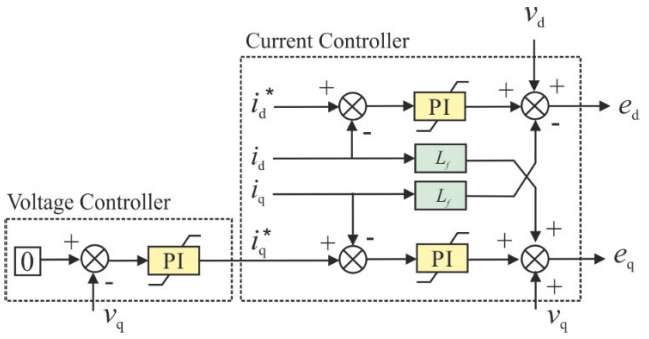

FIGURE 12. Outer voltage controller and Inner current controller.

The outer voltage controller maintains the voltage vector oriented by establishing that $v_q^* = 0$ by regulating the current, i_q. This is possible because the dynamic equations in the filter capacitor, C_f, describe the relationship between current and voltage in each of the dq axes. These equations, expressed in normalized values, are

$$\begin{aligned} i_d - i_{dg} &= \frac{C_f}{\omega_0}\frac{dv_d}{dt} - C_f v_q \\ i_q - i_{qg} &= \frac{C_f}{\omega_0}\frac{dv_q}{dt} + C_f v_d. \end{aligned} \tag{22}$$

The second equation in (22) demonstrates how the current, i_q, controls the variation of v_q, where the i_{qg} and $C_f v_d$ terms both represent voltage control loop disturbance variables. In the first equation, when the voltage is oriented toward the rotary reference system ($v_q = 0$), the current, i_d, matches i_{dg} in a steady state. Therefore, the GFC active power and power transmitted to the grid are equal. In a transient state, the difference between both currents modifies the voltage, v_d, which is equal to the PCC voltage magnitude. This proves that the PCC voltage magnitude can indeed be controlled through active power by changing the current reference i_d^*, but only when operating in islanding mode. When the GFC operates in an islanded mode, the voltage control through the active power is used to obtain the power demanded by the load. However, when the GFC is connected to a grid, the active power cannot be used to regulate PCC voltage because the power setpoint is only used to obtain a given amount of power from the source. Therefore, on grid-connected mode, the voltage is commonly controlled through the exchange of reactive power by modifying the Q_g^* value (Fig. 9). This reasoning, as per the filter capacitor equations, is also valid when the output filter of the GFC is type L [22], [25], [26].

C. REACTIVE POWER SYNCHRONIZATION BLOCK DIAGRAM

The voltage and current controllers specified in the previous section monitor the reference active power from i_d^* and maintain the voltage vector aligned to the reference system, which rotates at a speed of ω (Fig. 10); thus, $v_q^* = 0$. As the dynamics of these voltage and current regulators are faster than the dynamics of synchronization loop, it can safely assume that

$$i_d = i_d^* v_q = 0. \tag{23}$$

The dynamic equation of the current vector, $\boldsymbol{i}_{g,dq}$, expressed in pu is

$$\frac{L_g}{\omega_0}\frac{d\boldsymbol{i}_{g,dq}}{dt} = \boldsymbol{v}_{dq} - \boldsymbol{v}_{g,dq} - \left(R_g + jL_g\right)\boldsymbol{i}_{g,dq} \tag{24}$$

where $\boldsymbol{i}_{g,dq}$ represents the grid current vector along the dq axes.

Based on the conditions set forth in (23), the active and reactive power expressions in (6) are

$$\begin{aligned} P_g &= +v_d i_{dg} \\ Q_g &= -v_d i_{qg}. \end{aligned} \tag{25}$$

Taking the imaginary part of (24)

$$\frac{L_g}{\omega_0}\frac{di_{qg}}{dt} = -v_{qg} - R_g i_{qg} - L_g i_{dg}. \tag{26}$$

Furthermore, using the PCC voltage vector oriented toward the d axis as the reference, as denoted in Fig. 10, then $v_{qg} = -\left|\boldsymbol{v}_g\right| sin\delta$. Linearizing (26) around an operating point, this expression is reduced to

$$\frac{L_g}{\omega_0}\frac{d\Delta i_{qg}}{dt} = v_{g0} cos\delta_0 \Delta\delta - R_g \Delta i_{qg} - L_g \Delta i_{dg}. \tag{27}$$

This equation considers that $\Delta\omega = 0$. In other words, the frequency variation has not been taken into account because the equation assumes that the control system always maintains the voltage vector oriented. Moreover, (27) denotes the relationship between i_{qg} (reactive power) and the angle, δ. Assessing this expression in a steady state, disregarding the resistance R_g and multiplying by v_{d0}, the following relation is obtained:

$$\Delta P_g = \left(\frac{v_{g0} v_{d0}}{L_g} cos\delta_0\right)\Delta\delta \tag{28}$$

where the term in parentheses is the synchronization constant, $K_{p\delta}$.

From (27), a dynamic relationship between the reactive power and angle, δ can be established. Solving the equation for Δi_{qg} and using the operator, s, it is obtained that

$$\Delta i_{qg} = \frac{\omega_0}{\left(s + \frac{R_g}{L_g}\omega_0\right)}\left(\frac{v_{g0} cos\delta_0}{L_g}\Delta\delta - \Delta i_{dg}\right). \tag{29}$$

Starting from the hypothesis established in (23), and without considering the capacitor, C_f, dynamics, it can be deduced that $\Delta i_{dg} = \Delta i_d^*$. Therefore, if (27) is multiplied by v_{d0}, the following dynamic relation is obtained:

$$\Delta Q_g = \frac{\omega_0}{\left(s + \frac{R_g}{L_g}\omega_0\right)}\left(\Delta P_g^* - K_{p\delta}\Delta\delta\right) \tag{30}$$

where $\Delta P_g^* = v_{d0}\Delta i_d^*$. Likewise, the transfer function is also obtained:

$$G_{qp}(s) = \frac{\omega_0}{\left(s + \frac{R_g}{L_g}\omega_0\right)}, \tag{31}$$

which, as it may be observed, is equal to the relationship obtained between ΔP_g and ΔQ_g in (16) and (17). Fig. 13 illustrates the block diagram for the plant model and RPS controls from the previous equations.

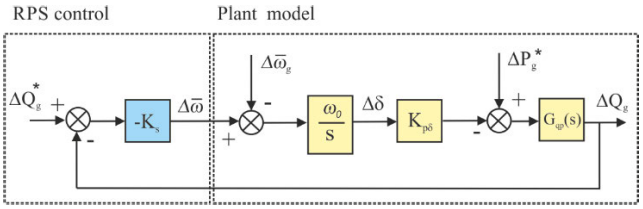

FIGURE 13. Block diagram RPS control and plant model.

The RPS control block determines the frequency increase for the reference rotary system, $\Delta\overline{\omega}$, based on the difference between the reference reactive power, ΔQ_g^*, and generated reactive power, ΔQ_g, using K_s as a synchronization constant. The difference between the frequency, $\Delta\overline{\omega}$, and grid frequency, $\Delta\overline{\omega}_g$, is integrated to obtain $\Delta\delta$ as per (21). The reactive power increase, ΔQ_g, is obtained from the transfer function (31) and difference between ΔP_g^* and $K_{p\delta}\Delta\delta$.

D. CHARACTERISTIC SWING EQUATION

To characterize the RPS procedure, the oscillation equation that relates the dynamic variation of $\Delta\delta$ against a change in ΔP_g^* has to be determined, as an analogy of what happens in an SG. Using the block diagram from Fig. 13, when $\Delta\overline{\omega}_g = 0$ and $\Delta Q_g^* = 0$,

$$\Delta P_g^* = \left(\frac{s}{G_{qp} K_s \omega_0}\right)\Delta\delta + K_{p\delta}\Delta\delta, \tag{32}$$

and considering (31), the oscillation equation is reduced to

$$\left(\frac{1}{K_s\omega_0^2}\right)s^2\Delta\delta + \left(\frac{R_g}{L_g K_s \omega_0}\right)s\Delta\delta + K_{p\delta}\Delta\delta = \Delta P_g^*. \tag{33}$$

The study of the classical model of an SG connected to an infinite bus [27] generates the following oscillation equation:

$$\left(\frac{2H}{\omega_0}\right)s^2\Delta\delta + \left(\frac{D}{\omega_0}\right)s\Delta\delta + K_{p\delta}\Delta\delta = \Delta P_m \tag{34}$$

where H is the inertia constant, and D is the damping coefficient. Comparing (34) and (33), then

$$H = \left(\frac{1}{2K_s\omega_0}\right) D = \left(\frac{R_g}{K_s L_g}\right). \tag{35}$$

The synchronization constant, $K_{p\delta}$, in both the equations are analogous. The H and D constants are inversely proportional to the synchronization constant, K_s. Based on the unit values used in Section III ($R_g = 0.01$ pu, $L_g = 0.15$ pu, and $\omega_0 = 100\pi$ rad/s) and a typical value of $K_s = 0.1$ pu [23], the inertia constant is $H = 0.016$ s and, the damping constant is $D = 0.67$ pu. The H value is extremely lower than the H value reported for an SG, whose typical values are several seconds. This large difference is explained by the inertia constant being produced through an electromagnetic effect, instead of an electromechanical effect as happens in an SG.

The following sections discuss the contribution from renewable generation plants to the inertia emulation and active power exchange capacities against frequency changes reported in a grid.

V. DC SOURCES MODELING AND CONTROL

Converters in grid-following mode operate as virtual SGs functioning as AC voltage sources connected to a grid (Fig. 3). In an islanded operation, the GFC supplies the power demanded by the load to maintain the voltage and frequency values at its terminals. The active power demanded by the load is supplied by the DC source, which is usually modeled as an ideal source of constant DC voltage in the literature. However, in actual converter operation, the source may be connected to the DC terminals of the converter, such as batteries, wind turbines, or PV generators.

For PV generators at a given irradiance and temperature conditions, the characteristic P(V) curve of the generator presents the maximum power generated at a given DC voltage, and the converter regulates the DC voltage to obtain the maximum power point (MPPT). An extensive literature exists on different MPPT techniques used for PV plants, including the perturbation and observation method [29]–[31], incremental conductance method [32]–[34], and others based on artificial neural networks and fuzzy logic [35]. GFCs may operate in PV plants connected to a grid using an MPPT strategy. However, in this case, they cannot engage in P/f regulation and supply power when a drop in grid frequency is detected as this requires additional power input that they are not able to generate because the maximum possible power has already been extracted from the panel. To provide this service, panels must operate at a DC voltage that exceeds their maximum power value, thus generating a lower power. Further, they can also store a power reserve that may allow them to increase power when demanded. When the DC voltage is lower than the maximum power voltage, less power is also generated, but the operations are conducted at a higher current, and therefore, at lower performance levels [36]. Obviously, this mode of operation is not economic although it may be required by grid codes in certain operating circumstances. When a PV generator supplies an islanded load, with sufficient solar resources, a simple open-loop control (leaving the DC voltage free) would allow the PV generator to automatically adjust the DC voltage to the level required for supplying the power demanded by the load. Of course, even when this technique may be possible, the most efficient way to supply an islanded load is using a hybrid system (PV generator + energy storage systems) [37], [38].

In variable-speed wind turbines, an MPPT strategy is also implemented, but, in this case, the rotation speed of the turbine is modified to extract the maximum possible power from the incident wind. This paper assesses a technology known as type IV or FC, which comprises two back-to-back converters. The converter connected to the machine (back-end converter) controls the electrical torque of the generator to regulate the rotation speed of the wind turbine based on an MPPT strategy that establishes a relationship between the maximum power and rotation speed of the turbine. The other converter (the front-end converter) is connected to the grid. This converter controls the DC voltage, thus guaranteeing that all the power generated by the turbine and injected into the DC bus is instantly drained into the grid. In the classic example of an FC wind turbine connected to a grid, the front-end converter works in grid-following mode using a PLL. This type of generator provides P/f regulation [39] and even emulates inertia as a virtual SG [40] through grid-supporting controls. Moreover, these generators can also operate in islanded mode [41] and can even provide black start services [42]. When a GFC is used in a converter connected to a grid, as illustrated in Fig. 1, the converter receives a power command. Further, the back-end converter controls the DC voltage through a regulation loop that determines the electrical torque of the generator. In this case, the functions of the back-to-back converters are interchanged from the classic control configuration. The main advantage of a GFC mode control is that the FC turbine may either operate connected to the grid or in an islanded mode. This latter mode of operation is not possible for grid-following converters. In an islanded mode, the front-end converter behaves as an AC voltage source, thus maintaining the voltage and frequency as constants at GFC terminals. The active power demand is transferred to the DC bus, which is served by the back-end converter, regulating the DC voltage while, in turn, modifying the power provided by the electric generator. As can be observed, in this operation mode, power flows are determined by the load and not by the primary energy source, as in grid-connected systems.

Below, the electrical models for each of the DC sources used are described, as well as the regulation strategy for the GFC–RPS in the both modes of operation: a) islanded and b) grid connected.

A. BATTERY MODEL

The electrical model of the battery [43]–[45], as illustrated in Fig. 14, includes a voltage source, E_b, which depends on the state of charge (SoC), a series resistor, R_s, and a capacitor, C_b, connected in parallel with the resistance, R_p, which represents the transient capacity of the battery.

When a sudden change occurs in the current, I_b, voltage variations at the battery terminals, V_{dc}, are not instantaneous but change based on a time constant, $\tau_b = R_p C_b$.

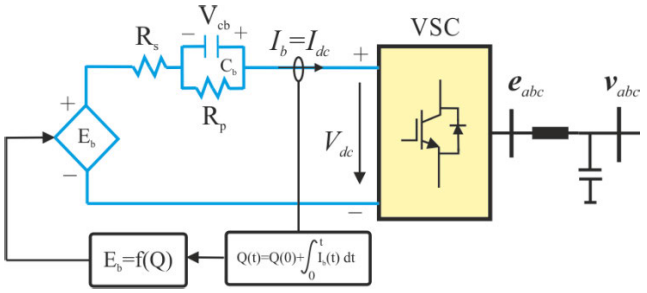

FIGURE 14. Equivalent circuit of a battery.

The SoC of the battery is defined as

$$SoC = 1 - \frac{Q(t)}{Q_n} \tag{36}$$

where Q_n represents its nominal capacity, and $Q(t)$ is the capacity discharged at a given time, which is calculated as

$$Q(t) = Q(0) + \int_0^t I_b dt. \tag{37}$$

The expression of the dependent voltage source, E_b, is calculated according to [38] as

$$E_b(t) = E_0 - K\frac{Q_n}{Q_n - Q(t)} + Ae^{-BQ(t)}. \tag{38}$$

The first term, E_0, corresponds to the nominal no-load voltage. The second term, which is expressed with a negative sign, is actually K/SoC and represents the voltage drop during discharge, where K is the polarization constant. As can be observed in Fig. 15, the drop is very pronounced when the battery is extremely discharged ($SoC \sim 0$). The third term represents the surge effect experienced by the battery when charged $SoC \sim 1$ and is modeled by the following exponential function: $Ae^{-BQ(t)}$. Table 1 of Appendix B lists the parameters that represent the discharge curve displayed in Fig. 15 according to (38).

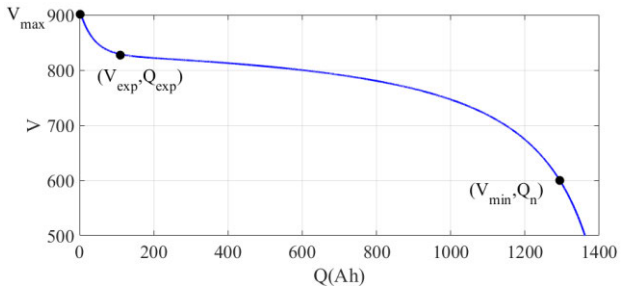

FIGURE 15. Discharge curve of the battery (Table 1).

The dynamic equations used to determine the voltage at the terminals of the battery, V_{dc}, are

$$\begin{aligned} \frac{dV_{cb}}{dt} &= -\frac{1}{C_b}\left(I_b + \frac{V_{cb}}{R_p}\right) \\ V_{dc} &= E_b + V_{cb} - R_s I_b. \end{aligned} \tag{39}$$

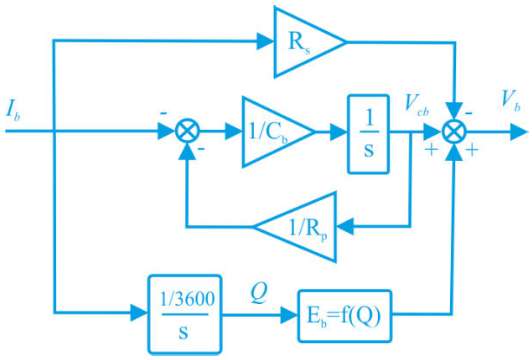

FIGURE 16. Battery block diagram.

Fig. 16 shows the block diagram for the battery considering both (36) and (37).

To assess the dynamic response from the battery against changes in power setpoint values or grid frequency variations, the E_b voltage can be considered constant if the assessment time period is short because the SoC of the battery only exhibits a slight variation. Fig. 15 denotes that, for a battery discharge capacity of 600 Ah, the recorded voltage is nominal, i.e., $V_n = 800$ V. Therefore, even if the battery is discharged at a current of 1 C (1200 A) for several seconds, the voltage variations in the battery are extremely small because the SoC of the battery only exhibits a slight variation.

B. FULL-CONVERTER GENERATOR MODEL

Fig. 2 (b) illustrates a type-IV wind turbine (full converter) up to the DC bus. In a conventional FC configuration, the back-end converter receives a torque command to regulate the rotation speed of the turbine. In a generator rotor flux-oriented control scheme, the torque is proportional to the q-axis current. Therefore, the d-axis current is usually set to zero to obtain a given torque from the minimum current [46]–[48]. In this case, the DC voltage is kept constant using a voltage regulator implemented in the front-end converter, which extracts all the active power produced by the generator.

Conversely, when a GFC is used, the power control of the wind turbine is implemented in the front-end converter. This way, the DC voltage is regulated by the back-end converter. The output from this regulator is the current, I_{fc}, as shown in Fig. 17, which is proportional to the active power of the generator. Unlike conventional FC controls, the active power generated first passes from the front-end converter to the generator and then to the turbine.

The simplified electrical model for the FC turbine (type IV) depicted in Fig. 12 (b) is represented by a dependent current source whose value is the output of a DC voltage regulator, as specified in Fig. 17. The current, $I_{fc,}$ is calculated based on the voltage error, $e_{dc} = V_{dc}^* - V_{dc}$, as

$$I_{fc} = k_{pv}e_{dc} + k_{pi}\int e_{dc}dt. \tag{40}$$

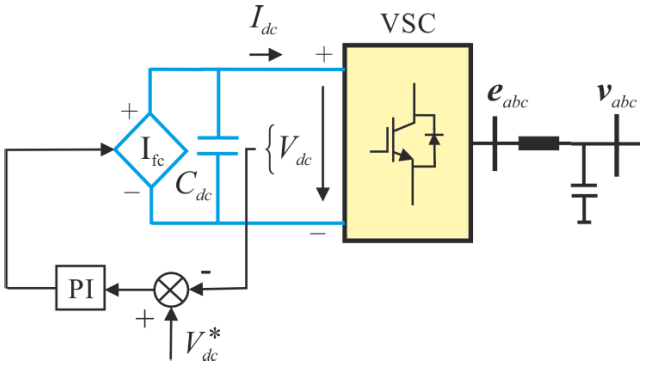

FIGURE 17. Back-end converter equivalent circuit of a full converter using a GFC.

The voltage response, V_{dc}, is obtained from the dynamic equation for the capacitor, C_{dc} :

$$\frac{dV_{dc}}{dt} = \frac{1}{C_{dc}}\left(I_{fc} - I_{dc}\right) \tag{41}$$

Assuming that no losses exist in the front-end converter, and the voltage vector is oriented toward the d axis of the rotary reference system, the following relationship is given according to [49]:

$$I_{dc} = \frac{3}{4} m_a i_d \tag{42}$$

where m_a is the amplitude modulation index, and i_d is the direct component of the current vector at the output of the converter.

C. GFC CONTROL. BATTERY AND FULL CONVERTER

The GFC–RPS control scheme proposed herein is applicable when a battery is connected to the DC terminals of the front-end converter or to the back-end converter of a wind turbine modeled as a dependent current source, as shown in Fig. 17.

The inputs of the control system are as follows: a) the reference current, i_d^*; and b) reference reactive power, Q_g^*, incoming to the RPS block.

The i_d^* component has three terms as can be observed in the following expression:

$$i_d^* = i_d^{ref} - \frac{\Delta\overline{\omega}}{R} + i_d^{hs}. \tag{43}$$

The first term is the i_d^{ref} component corresponding to the reference active power, P_g^*. In per unit values, i_d^{ref} is calculated as the quotient between P_g^* and the voltage modulus of GFC terminals, v_d. Here, it has to be pointed out that $v_q = 0$ applies for the voltage controller; therefore, $|v| = v_d$. The second term is calculated from the frequency increase, $\Delta\overline{\omega}$, obtained as an internal variable from the RPS block and multiplied by the inverse of the droop constant, R. When a frequency drop is detected ($\Delta\overline{\omega} < 0$)), the GFC injects additional active power by increasing the value of i_d^*. Note the minus sign of the second term in (43). The third term is only used when the converter operates in an islanded mode, and it corresponds to the reference current, i_d^{hs}, obtained from the AC voltage control block and uses a hot-swapping mechanism between the grid-following operation and islanded modes. This block establishes a voltage control at GFC terminals when they become disconnected from the grid and start operating in an islanded mode. The voltage control in an islanded mode is conducted through the current, i_d, as demonstrated in (22). However, when the GFC is connected to a grid, the voltage depends on the short-circuit impedance at the PCC and on the amount of reactive power exchanged. In Fig. 18, the GFC contributes to AC voltage regulation when the converter is connected to the grid through Q_g^* using a droop constant, n_Q.

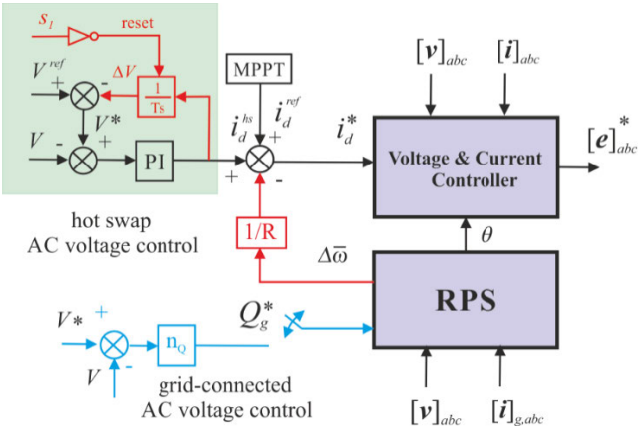

FIGURE 18. GFC control diagram of a VSC when a battery or a full converter is connected on the DC bus.

In the AC voltage control block with a hot-swapping mechanism, when the GFC is connected to the grid, the reference AC voltage, V^{ref}, is not required to match the voltage, V, recorded at the terminals. In this case, $i_d^{hs} \neq 0$ current is generated, which is corrected by subtracting a voltage increase, ΔV, from V^{ref} so that $V^* = V^{ref} - \Delta V$. The increase in voltage, ΔV, is calculated using a slow integral regulator until $V^* = V$ and $i_d^{hs} = 0$. This regulator has a reset signal that is only triggered when the output switch is open (s_1 off). In this situation, the integrator block is disabled, and ΔV becomes null. When the GFC operates in an islanded mode, the voltage is controlled through the injection of active current, i_d^{hs}, at the terminals.

This control block allows the hot-swapping mechanism to control the AC voltage when the grid-connection trips. During the grid disconnection process, the capacitor voltage tends to decrease rapidly. For this reason, the reference voltage takes a value exceeding the nominal value to compensate this drop dynamically, e.g., $V^{ref} = 1.05$ pu.

D. PV GENERATOR MODEL

The PV generator model depicted in Fig. 19 corresponds to a Norton equivalent, where, according to [36], the current

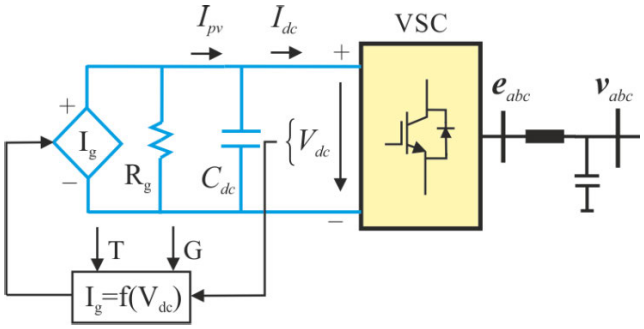

FIGURE 19. PV generator equivalent circuit.

source, I_g, and resistance, R_g, are

$$I_g = N_p I_i \left(\frac{R_{s,pv}}{R_{s,pv} + R_{p,pv}} \right)$$
$$R_g = \frac{N_s}{N_p} \left(R_{s,pv} + R_{p,pv} \right) \quad (44)$$

where $R_{s,pv}$ and $R_{p,pv}$ are the series and parallel resistances, respectively, of the ideal PV module. The number of modules connected in series forming a single string is N_s, and the number of strings connected in parallel is N_p.

According to [36], the current, I_i, at the module terminals is

$$I_i = I_{ph} - I_0 \left[exp \left(\left(\frac{R_{p,pv}}{R_{s,pv} + R_{p,pv}} \right) \frac{V_{pv} + R_s I_i}{\alpha V_{th}} \right) - 1 \right]. \quad (45)$$

The current, I_i, is a function of the voltage at the terminals of the PV module, V_{pv}, and of the current, $I_{ph} = f(G, T)$, wherein $G(\mathrm{W/m^2})$ represents the irradiance and T ($^{\circ}C$) the temperature. The current, I_0, is approximately equal to the short-circuit current of the PV module, where α is the ideality factor and V_{th} the thermal voltage.

Fig. 20 denotes the I(V) and P(V) curves for the PV generator assessed in the present study. The $P_{dc,max}$ maximum power is 2 MW (point A), and it is obtained at a voltage of $V_{dc,max} = 700$ V.

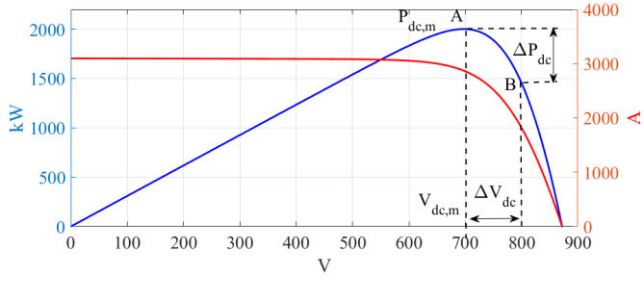

FIGURE 20. I(V) and P(V) curves of a PV generator.

Table 2 of Appendix B hereto lists the corresponding PV generator parameters.

E. GFC CONTROL PV GENERATOR

In the same manner as the battery and FC turbine, the GFC control for the PV generator also uses the current, i_d^*, and reactive power, Q_g^*, as input variables, whose values can be determined using an outer AC voltage controller. The difference of this GFC is that a reference active power cannot be imposed from the front-end converter, but it is imposed through a voltage control, V_{dc}, following a PV generator MPPT strategy (point A in Fig. 20).

The PV generator can provide the power/frequency (P/f) regulation service as long as it does not operate at its maximum power point, $P_{dc,max}$, thereby reducing the power generated at a constant value of ΔP_{dc} through a delta control. Fig. 21 denotes the control scheme required by the PV generator to effectively provide P/f regulation services. Initially, $P_{dc,max}$ is determined through an estimator using the temperature and irradiance as input variables. Thereafter, the power increase, ΔP_{dc}, is subtracted from this power so that power may be increased if there is a frequency drop. The maximum power estimator also determines the value of the voltage , $V_{dc,max}$, at which $P_{dc,max}$ is generated. The voltage, $V_{dc,max}$, is the lower limit of the integral regulator that determines the reference voltage, V_{dc}^*, of the PV generator. The maximum regulator limit corresponds to the no-load voltage, V_{oc}, whose value is specified in Table 2 of Appendix B. Finally, the DC voltage regulator determines the reference, i_d^*, for the GFC. The time constant of the integral regulator is adjusted so that it can be slower than the response from the DC voltage regulator. In this case, a value of $T = 0.5$ s is used.

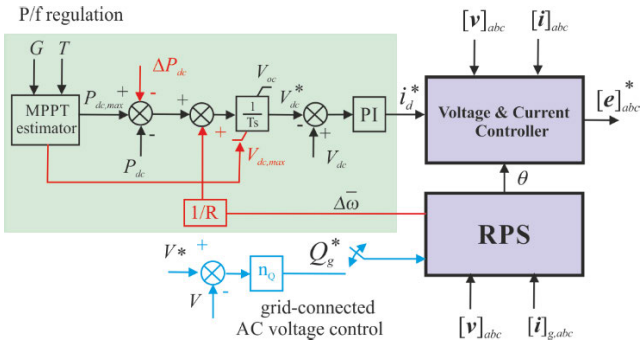

FIGURE 21. GFC control diagram of a PV generator during P/f regulation.

In P/f regulation, a ΔP_{dc} power reserve is deliberately imposed so that it can be applied if the grid experiences a frequency drop ($\Delta\bar{\omega} < 0$). The regulation loop generates an increase in $-\Delta\bar{\omega}/R$ power, which results in a transient V_{dc}^* voltage drop, thus increasing the additional reference current, i_d^*. Otherwise, against an increase in frequency ($\Delta\bar{\omega} > 0$), the reference, i_d^*, drops, generated power decreases, and DC voltage transiently increases. Once $\Delta\bar{\omega} = 0$, the DC reference voltage returns to its initial setpoint value. The PV generator provides these P/f regulation services in the operating area wherein the voltage, $V_{dc,}$ exceeds $V_{dc,max}$.

VI. VOLTAGE AND CURRENT CONTROLLERS TUNING

The control system features two nested control loops, an inner current loop, and an outer voltage loop. The current loop is formed through a PI regulator that controls a plant represented by a first-order function as per the dynamics of the L_f filter. Here, the open-loop transfer function of the current controller is

$$G_c(s) = k_{pc}\left(\frac{T_c s + 1}{T_c s}\right)\left(\frac{1/R_f}{T_f s + 1}\right) \tag{46}$$

where k_{pc} is the proportional gain of the regulator, and T_c its integral time constant. The time constant of the filter is $T_f = L_f/(\omega_b R_f)$, where L_f and R_f represent the inductance and resistance of the filter in pu, respectively, and ω_b represents its base frequency in rad/s. According to the filter parameters detailed in Table 3 of Appendix C, $T_f = 95$ ms. If the time constant of the regulator equals the time constant of the plant, i.e., $T_c = T_f$, the pole-zero pair of the transfer function is cancelled out, and (45) remains as an integral function expressed as

$$G_c(s) = k_{pc}\left(\frac{\omega_b}{L_f}\right)\frac{1}{s}. \tag{47}$$

The transfer function of the closed-loop current controller, G'_c, is calculated as

$$G'_c = \frac{G_c}{1 + G_c} = \frac{1}{\tau_i s + 1} \tag{48}$$

where $\tau_i = L_f/(\omega_b k_{pc})$.

The bandwidth of (47) corresponds to the $1/\tau_i$ value. The bandwidth (BW) selected for the current controller is 500 rad/s ($\tau_i = 2$ ms) so that $k_{pc} = 0.24$ pu considering that $L_f = 0.149$ pu and $\omega_b = 100\pi$ rad/s (see Appendix C). Fig. 22 denotes the Bode diagram for the transfer function of the closed-loop current controller.

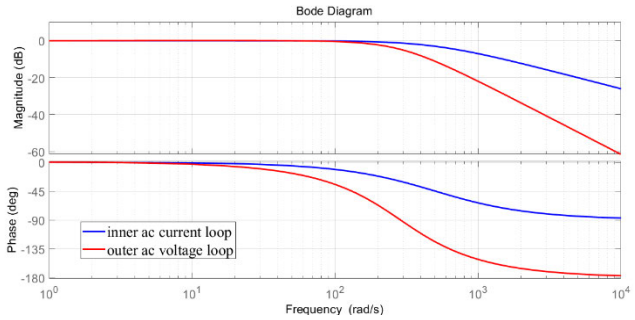

FIGURE 22. Bode diagram of the inner AC current loop (500 rad/s bandwidth) and of the outer AC voltage loop (250 rad/s bandwidth).

The outer AC voltage regulator is calculated similarly. In this case, the open-loop transfer function would be

$$G_v(s) = k_{pv}\left(\frac{T_v s + 1}{T_v s}\right)\left(\frac{1}{\tau_i s + 1}\right)\left(\frac{1}{T_{c,ac} s}\right). \tag{49}$$

The G_v function has three terms. The first one corresponds to the transfer function of the PI regulator, where k_{pv} and T_v are the proportional gain and integral time constant, respectively. The second term is the transfer function from (47), and the third term is the transfer function for the plant based on the dynamics of the capacitor, where $T_{c,ac}$ is its time constant calculated as the product from multiplying the filter capacity by the value of the base AC impedance, $T_{c,ac} = C_f Z_{b,ac}$. Based on the values specified in Table 3 of Appendix C, $C_f = 6$ mF, $Z_{b,ac} = 0.08\Omega$, and the time constant, $T_{c,ac}$, is 0.48 ms.

The regulator design uses $T_v = 4T_c$ and a voltage regulator bandwidth of 250 rad/s (50% of the current loop bandwidth). At these values, the proportional constant for the voltage regulator is $k_{pv} = 0.1$ pu. The Bode diagram for the transfer function of the closed-loop current controller is illustrated in Fig. 22.

This same procedure is followed when calculating the DC voltage regulator. In this case, the time constant of the DC capacitor, $T_{c,dc}$, is given by $C_{dc}Z_{b,dc}$. According to the parameters from Table 3 (Appendix C), the capacitance of the DC capacitor is $C_{dc} = 150$ mF, and its impedance is $Z_{b,dc} = (8/3)Z_{b,dc}$ [36], which means that $T_{c,dc} = 32$ ms. Applying the same methodology as above, the proportional gain of the DC voltage regulator is now equal to $k_{pv} = 5.4$ pu and generates a bandwidth of 250 rad/s.

VII. SIMULATION RESULTS

This section presents the results from the GFC converter simulation using the control strategies described in the previous sections. As shown in Fig. 23, the GFC is connected to the grid through the switch, s_1, and to a local dynamic load (AC motor). The generic DC source either represents a battery, FC wind turbine, or a PV plant

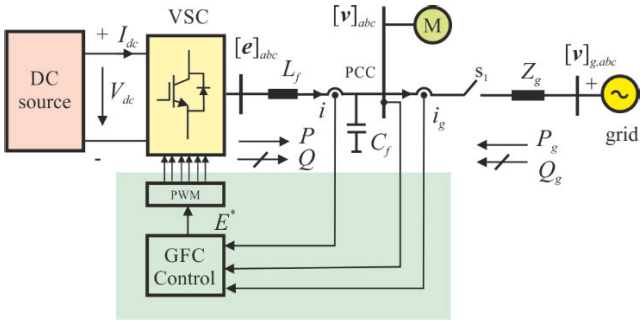

FIGURE 23. System description of a GFC connected to an AC grid by an s_1 switch and to a local dynamic load (AC motor). The generic DC source represents a battery, a full converter or a PV plant.

The simulation results have been grouped into three blocks. The first block examines the rapid response from the GFC against grid frequency changes depending on the source connected to its DC terminals. The second block discusses the contribution from the GFC to voltage control through reactive power regulation. Finally, the last block assesses the dynamic response from the GFC during the AC voltage control hot-swapping process when the GFC becomes disconnected from the grid, and the converter remains in an islanded mode

supplying a dynamic load at its terminals. All grid and dynamic load parameters are listed in Table 3 of Appendix C.

A. FAST FREQUENCY RESPONSE

This section examines the response from the GFC and different DC sources after a load change. For these purposes, we are considering a dynamic grid represented by an SG with an inertia constant of $H = 4$ s, a droop constant of $R = 5\%$, and an integral constant of $K_I = 0.1$ pu to perform secondary regulation. The SG and GFC feed a load of 90 MW. At $t = 1$ s, this load increases to 108 MW, which causes a frequency deviation, as observed in Fig. 24. Because the power contribution from each of the DC sources is different, the frequency values recorded are different.

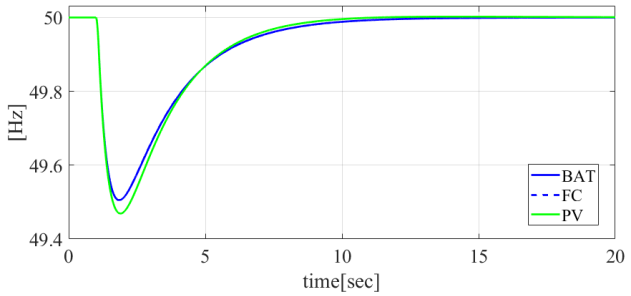

FIGURE 24. Frequency response after a load change.

Here, at t = 1 s, a grid frequency drop occurs that reaches 49.5 Hz ($\Delta\overline{\omega} = 1\%$), but it gradually recovers through the action of the secondary regulation services until again reaching its nominal value at t = 15 s. The droop constant used for this fast frequency response (FFR) strategy is the same droop constant of the grid, i.e., $R = 0.05$ pu.

This response is only reported in the control strategy for a GFC connected to a battery or to a FC turbine (Fig. 18), where the current, i_d^*, corresponding to a frequency variation is calculated according to (43) as $-\Delta\overline{\omega}/R$. Fig. 25 denotes the power response from the GFC connected to the different DC sources assessed after the grid has experienced a load change. For the battery and FC wind turbine, the maximum power increases to 370 kW, which gradually reduces as the frequency recovers. As can be observed, the response from both the systems is practically the same. According to the control scheme discussed in Section V (item E), the response from the PV plant is also shown in Fig. 25. The maximum power increase generated is less than the one reported for the battery and FC wind turbine (170 kW). Therefore, causing a higher frequency deviation. This variation in power is lower because of the dynamics of power being controlled through the DC voltage controls in the PV generators. Fig. 25 also shows how the reactive power, Q_g, (in red) follows the frequency variations experienced by the grid to maintain synchronism although the reference value is $Q_g^* = 0$. The minimum reactive power value recorded is 500 KVAr.

Fig. 26 displays the V_{dc} variation from all the three DC voltage sources. For the battery, after a sudden change in

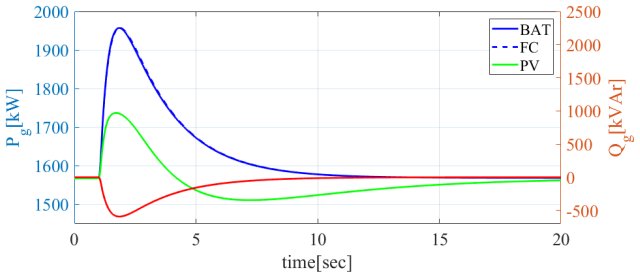

FIGURE 25. GFC active and reactive power response during a load change in the grid for different DC sources.

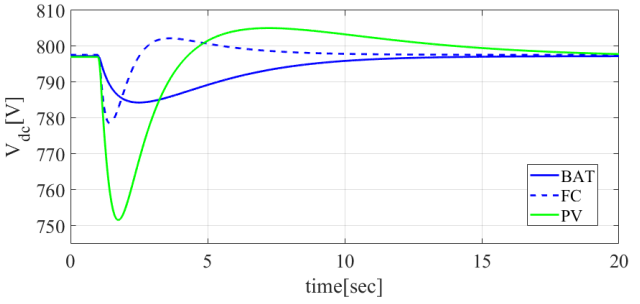

FIGURE 26. DC sources voltage response during a frequency change in the grid.

frequency, the voltage drops by capacitive effect to 785 V and recovers until it reaches its initial value at $t = 20$ s. The DC voltage behavior experienced by the FC turbine denotes a similar drop, but its dynamics are faster, even exceeding 800 V during the voltage recovery process, which finally stabilizes at 20 s. For the PV plant, the voltage is reduced to 750 V but then overshoots exceeding 800 V. Therefore, the active power delivered is at times lower than the initial power (Fig. 25).

B. REACTIVE VOLTAGE DROOP CONTROL

When the GFC is connected to the grid, AC voltage is controlled based on the reference reactive power, Q_g^*, from the RPS loop. Fig. 27 charts the response from the GFC after a voltage increase in the grid at t = 0.5 s until the voltage reaches 1.09 V at the terminals. The droop control shown in Fig. 18 and Fig. 21 causes the GFC to respond before a voltage increase in the grid by absorbing 1 MVAr. This analysis demonstrates how the GFC is able to contribute to AC voltage control by exchanging reactive power, Q_g, even when this variable is also used in the synchronization loop. The real AC voltage control depends on the short-circuit power of the grid. Consequently, when the short-circuit ratio is high, a considerable reactive power must be exchanged to modify the voltage at the GFC terminals.

C. HOT SWAP FROM GRID CONNECTED TO ISLANDED

The transition between grid-connected and islanded modes of operation is one of the requirements demanded from GFCs when operating as voltage sources. However, this transition can lead to significant voltage and frequency

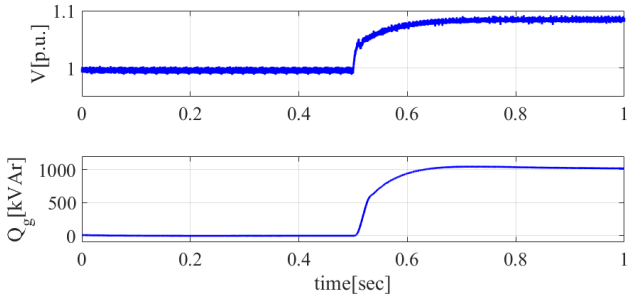

FIGURE 27. GFC reactive power response under an AC voltage increment.

variations at converter terminals when the converter swaps from a grid-following to an islanded mode, especially after a dynamic load has been supplied. This section discusses the dynamic response from the GFC under the hot-swapping control strategy, as denoted in Fig. 18, after a grid disconnection at $t = 0.5$ s, and the converter supplies a dynamic load.

For these purposes, it is assumed that the GFC is connected to a battery at its DC terminals. The GFC is coupled to the grid at its AC terminals, where an induction motor is also connected. The characteristics of this induction motor are described in Table 3 of Appendix C. The motor demands 1 MW, which is supplied from the grid, because the i_d^* setpoint of the converter is zero. Similarly, the reference reactive power based on the input from the RPS block is $Q_g^* = 0$. Therefore, the converter provides the reactive power demanded by the motor that it is not compensated by the capacitors, C_f, of the LC filter.

The GFC control strategy is specified in Section V (item C). The RPS block synchronizes the GFC to the grid while maintaining $v_q = 0$. The v_d voltage regulator also remains active, with the integrator enabled with a time constant of $T = 0.3$ s enabled to adjust the V^* reference to the actual voltage of the grid ($v_d = 1$ pu). The V^{ref} voltage is set at a higher value than the rated voltage, which is 1.05 pu. This way, in a steady state, $\Delta V = 0.05$ pu, and the current is $i_d^{hs} = 0$. The top chart in Fig. 28 shows the voltages, v_d and v_q, when the main switch, s_1, trips at $t = 0.5$ s.

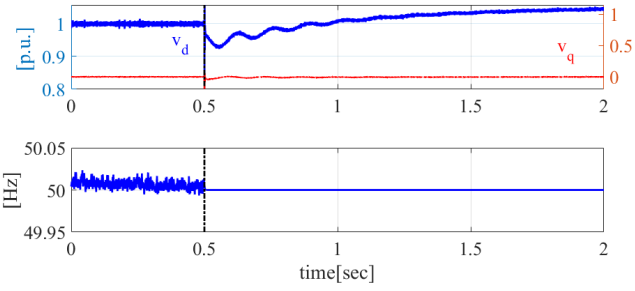

FIGURE 28. Voltage and frequency response during the transition between grid-connected mode to is landed mode.

The voltage across the capacitor tends to drop rapidly when the grid is disconnected, at which point the voltage regulator, v_d, acts by injecting the current, $i_d^{hs} \neq 0$. The reference voltage increase, V^{ref}, described above, is conducted precisely to compensate the voltage drop in the first moments after the switch has tripped. In Fig. 28, the voltage magnitude drops to 0.9 pu and then recovers to its setpoint value of $V^{ref} = 1.05$ pu in $t = 2$ s. The grid frequency oscillates around 50 Hz before the switch trips due to the instantaneous reactive power ripple. However, after a disconnection, with the GFC hot swapping to islanded mode, the frequency imposed by the control system is exactly 50 Hz. This is caused because the frequency, $\Delta\overline{\omega}$, is equal to zero, which, in turn, occurs because $Q_g^* = 0$ and the reactive power output is zero when the switch trips. The bottom chart in Fig. 28 denotes the frequency measured at the converter output terminals.

Fig. 29 displays the three-phase voltages at the output terminal of the GFC right before and after the switch trips. As can be observed, the voltage is slightly distorted in each phase, but the transition is smooth. Fig. 30 details the instantaneous voltage in one phase of the converter, e_a, and at its output terminals, v_a.

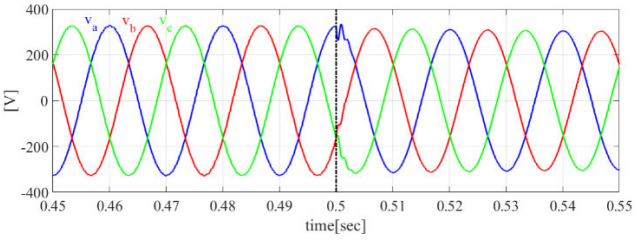

FIGURE 29. Instantaneous voltages in the three phases at the GFC output terminals.

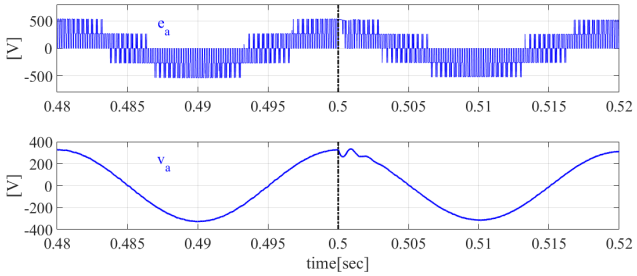

FIGURE 30. Instantaneous voltages in one phase at the GFC output e_a (top figure) and in its terminals v_a (bottom figure).

The output voltage of the converter presents the typical pulse width modulation shape. When the switch trips, a discontinuity is observed in the commutation that causes a slight distortion of the instantaneous voltage, v_a.

In an islanded mode of operation, the GFC maintains the voltage and frequency under control, only generating the active and reactive powers demanded by the load. Fig. 31 denotes the evolution of the active power generated by the converter, P, and power of the grid, P_g, during the grid disconnection process and its subsequent islanded operation supplying the motor. Before the switch trips, the active power

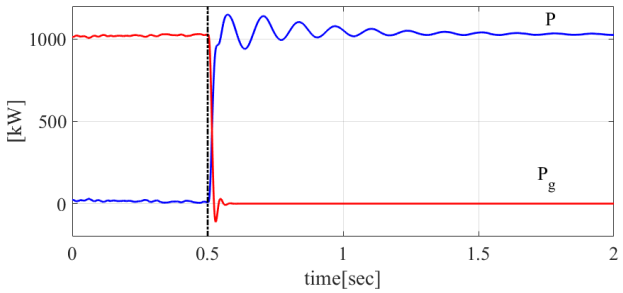

FIGURE 31. Active power drawn from the grid, P_g and active power generated by the GFC, P.

demanded by the load (1 MW) is supplied by the grid, and the GFC power setpoint is $i_d^* = 0$. After the switch trips, the grid power becomes zero, i.e., $P_g = 0$, and the GFC automatically assumes the motor load with a power oscillation caused by the changes produced in the voltage magnitude (Fig. 28).

Fig. 32 denotes the reactive power variation absorbed from the grid, Q_g, and generated by the converter, Q. The reference reactive power, Q_g^*, of the grid is zero at all times. Before the switch trips, Q_g assumes a value slightly higher than zero because the frequency is not strictly equal to 50 Hz, as shown in Fig. 28. The power, Q, supplied by the converter is 65 kVAr, which corresponds to the reactive power demanded by the motor minus the power supplied by the filter capacitors, C_f. After being disconnected from the grid, the power, Q_g, is zero (the current, i_g, is zero), and the reactive power supplied by the GFC undergoes an oscillation due to the transient voltage variation experienced at the terminals. At $t = 2$ s, the oscillation is dampened, thus reaching the same value of Q just before the switch trips.

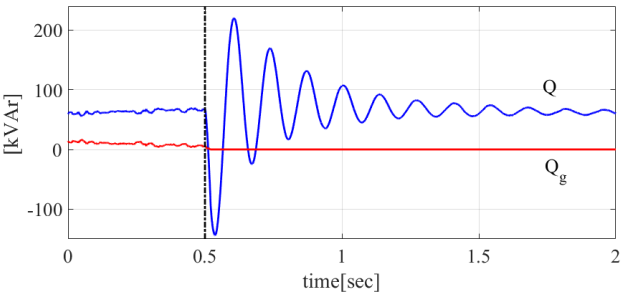

FIGURE 32. Reactive power drawn of the grid, P_g and reactive power generated by the GFC, P.

The instantaneous currents of the converter and grid are shown in Fig. 33 and Fig. 34, respectively. Before being disconnected, at $t = 0.5$ s, the converter injects only reactive current, and the active current demanded by the motor is supplied by the grid. After the switch, s_1, trips and the converter is disconnected from the grid, the current of the grid becomes zero, and the current of the converter increases to supply the active and reactive powers demanded by the motor.

The response from the motor is presented in Fig. 35. Before the grid switch trips, the motor rotates at 1457 rpm and

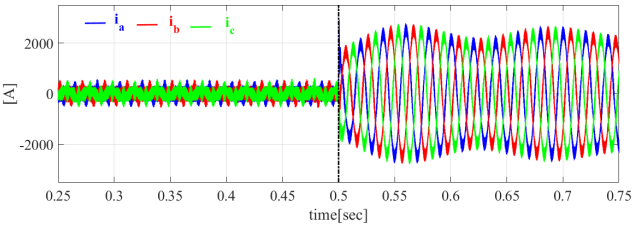

FIGURE 33. GFC instantaneous three-phase currents.

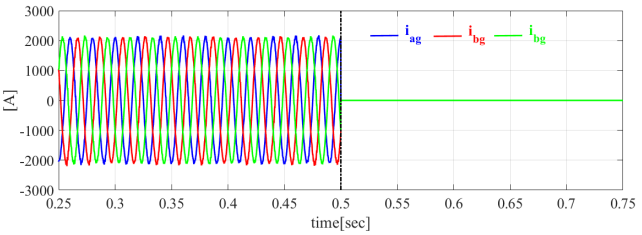

FIGURE 34. Instantaneous three-phase currents on the grid.

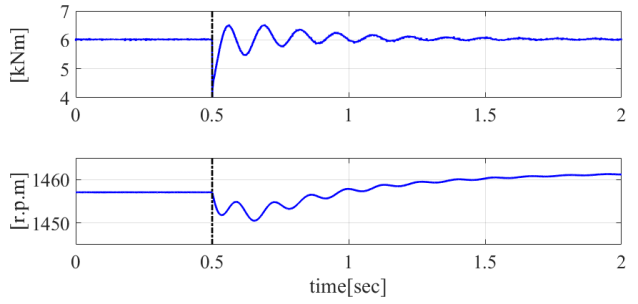

FIGURE 35. Response of the motor during the transition between grid-connected mode to an is landed mode. Electromagnetic torque (top figure) and rotational speed (bottom figure).

develops an electromagnetic torque of 6 kNm. In the moments after $t = 0.5$ pu, the torque oscillates, and the rotation speed initially drops and stabilizes at 1460 rpm at $t = 2$ s due to the increased voltage at the motor terminals, i.e., $V = 1.08$ pu.

The results presented in this section validate the robustness of the GFC–RPS control based on the hot-swapping strategy during the transition from a grid-connected mode to an islanded mode.

VIII. CONCLUSION

This study proposes a new GFC control system based on the RPS method applied to renewable energy plants: PV plants, FC wind turbines, and batteries. First, this paper provides an overview of the RPS method, discussing the dynamic coupling between the instantaneous active and reactive powers and transfer function between ΔQ_g and $\Delta\delta$, which allows the execution of the synchronization process.

Compared to other APS methods, the main advantage of this method is that it allows the decoupling of the active power control and synchronization loops, which facilitates the efficient integration of the different generation sources connected to the DC input bus.

TABLE 1. Li-ion battery parameters.

PARAMETER	SYMBOL	VALUE	UNITS
Maximum voltage	V_{max}	900	V
Nominal voltage	V_n	800	V
Minimum voltage	V_{min}	600	V
Exponential voltage	V_{exp}	825	V
Nominal capacity	Q_n	1300	Ah
Exponential capacity	Q_{exp}	100	Ah
Battery constant voltage	E_0	858	V
Polarization voltage	K	38.5	Ah
Exponential zone amplitude	A	81	V
Exponential zone time constant inverse	B	0.03	Ah^{-1}
Internal resistance	R_s	16	$m\Omega$
Capacitance	C_b	85	F
Parallel resistance	R_p	22.5	$m\Omega$

TABLE 2. PV generator parameters.

PARAMETER	SYMBOL	VALUE	UNITS
Maximum power	$P_{dc,max}$	2000	kW
Maximum power voltage	$V_{dc,msx}$	700	V
Open circuit voltage	V_{oc}	872	V
Short-circuit current	I_{sc}	3098	A
Series resistance	R_s	5.88	Ω
Parallel resistance	R_p	11	kΩ
Norton impedance	R_g	29.75	Ω
DC capacitance (*)	C_{dc}	150	mF
Number of modules in series	N_s	27	
Number of strings in parallel	N_p	370	

(*) same value as for the full converter

TABLE 3. Parameters used in the study.

PARAMETERS	SYMBOL	VALUE	UNITS	PU
Converter rated power	S_n	2000	kVA	1.00
Line to line rated voltage (RMS)	V_n	400	V	1.00
Filter inductance	L_f	38	μH	0.149
Filter resistance	R_f	0.4	$m\Omega$	0.005
Filter capacitance	C_f	6	mF	0.150
Nominal frequency	f_n	50	Hz	1.00
Switching frequency	f_{sw}	3	kHz	60
Synchronization constant	K_s	0.75	$Hz/MVAr$	0.03
Grid inductance	L_g	5.0	μH	0.019
Grid resistance	R_g	0.156	$m\Omega$	0.002
Short-circuit ratio	SCR	50		
X/R ratio	X/R	10		
Motor rated power	$P_{n,m}$	1000	kW	1.00
Phase rated voltage (RMS)	$V_{n,m}$	230	V	1.00
Stator resistance	R_s	11.84	$m\Omega$	0.074
Rotor resistance (*)	R'_r	4	$m\Omega$	0.025
Stator winding leakage	$L_{\sigma s}$	16.5	μH	0.032
Rotor winding leakage (*)	$L'_{\sigma r}$	16.5	μH	0.032
Magnetizing inductance	L_m	1.5	mH	2.946
Number of poles	P	4		
Moment of inertia	J	50	$kg \cdot m^2$	
Inertia constant	H	0.6	sec	

(*) referred to stator

Furthermore, this paper introduces different models and control schemes for PV plants, FC wind turbines, and batteries coupled to a GFC converter. Thereafter, the study proposes a GFC–RPS control scheme and verifies its effectiveness in different applications. The first application is P/f regulation when the grid experiences a load variation event. This service is provided with batteries and FC wind turbines through FFR from the internal control variable, $\Delta\overline{\omega}$. For PV plants, this service can only be provided if the power generated initially is lower than that of the maximum power point. In conclusion, PV plants can provide this service but a significant energy yield will be lost, with extreme economic implications.

Subsequently, in a grid-following mode, this paper proves the capabilities exhibited by the GFC–RPS control to exchange reactive power with the grid against voltage variations at its terminals, which also demonstrates the ability of the proposed system to control the AC voltage in the output terminals by exchanging reactive power, even when this variable is linked to the synchronization loop.

Finally, the excellent dynamic response of the GFC is validated in the transition process from a grid-connected mode to an islanded mode while supplying a dynamic load. The results revealed that both the voltage and frequency remain stable at the transition, thus demonstrating that the proposed GFC control indeed acts as a true voltage source emulating the behavior of a conventional SG.

APPENDIX A
STATE-SPACE MODEL MATRICES

Matrix A is expressed in (7). Matrix B is obtained from (5) as

$$B = \begin{bmatrix} cos\delta_0 & -V_0 sin\delta_0 \\ sin\delta_0 & +V_0 cos\delta_0 \end{bmatrix}.$$

Likewise, matrices C and D are obtained from the P_g and Q_g expressions in (6)

$$C = V_0 \begin{bmatrix} cos\delta_0 & sin\delta_0 \\ sin\delta_0 & -cos\delta_0 \end{bmatrix}$$

$$D = \begin{bmatrix} \frac{P_{g0}}{V_0} & -Q_{g0} \\ \frac{Q_{g0}}{V_0} & +P_{g0} \end{bmatrix}.$$

All quantities with a subscript of ''0'' indicate steady-state values calculated at the initial point.

APPENDIX B
DC SOURCES PARAMETERS

The battery definition parameters from Fig. 14 and Fig. 15 are listed in Table 1.

The PV generator parameters are shown in Table 2.

APPENDIX C
GRID AND CONVERTER PARAMETERS

Table 3 indicates the electronic converter, AC motor, and grid parameters used in this study.

REFERENCES

[1] R. H. Lasseter, ''Microgrids,'' in *Proc. IEEE Power Eng. Soc. Winter Meeting Conf.*, vol. 1, Jan. 2002, pp. 305–308.

[2] J. Rocabert, A. Luna, F. Blaabjerg, and P. Rodriguez, ''Control of power converters in AC microgrids,'' *IEEE Trans. Power Electron.*, vol. 27, no. 11, pp. 4734–4749, Nov. 2012.

[3] P. Christensen, G. K. Andersen, M. Seidel, S. Bolik, S. Engelken, T. Knueppel, A. Krontiris, K. Wuerflinger, T. Bülo, J. Jahn, and M. Ndreko, "High penetration of power electronic interfaced power sources and the potential contribution of grid forming converters," ENTSO-E, Brussels, Belgium, Tech. Rep. 1, 2020.

[4] *Establishing a Network Code on Requirements for Grid Connection of Generators*, Commission Regulation (EU) 2016/631, Brussels, Belgium, 2016.

[5] N. Hatziargyriou, "Task force on definition and characterization of dynamic behavior in systems with high penetration of power electronic interfaced technologies," Power Energy Soc., Piscataway, NJ, USA, Tech. Rep. PES-TR77, 2020.

[6] B. Yu, M. Matsui, and G. Yu, "A review of current anti-islanding methods for photovoltaic power system," *Sol. Energy*, vol. 84, no. 5, pp. 745–754, May 2010.

[7] R. Teodorescu, M. Liserre, and P. Rodriguez, *Grid Converters for Photovoltaic and Wind Power Systems*, vol. 29. Hoboken, NJ, USA: Wiley, 2011.

[8] A. Luna, J. Rocabert, J. I. Candela, J. R. Hermoso, R. Teodorescu, F. Blaabjerg, and P. Rodriguez, "Grid voltage synchronization for distributed generation systems under grid fault conditions," *IEEE Trans. Ind. Appl.*, vol. 51, no. 4, pp. 3414–3425, Jul. 2015.

[9] M. Karimi-Ghartemani, "A unifying approach to single-phase synchronous reference frame PLLs," *IEEE Trans. Power Electron.*, vol. 28, no. 10, pp. 4550–4556, Oct. 2013.

[10] X. Wang and F. Blaabjerg, "Harmonic stability in power electronic-based power systems: Concept, modeling, and analysis," *IEEE Trans. Smart Grid*, vol. 10, no. 3, pp. 2858–2870, May 2019.

[11] M. G. Taul, X. Wang, P. Davari, and F. Blaabjerg, "An overview of assessment methods for synchronization stability of grid-connected converters under severe symmetrical grid faults," *IEEE Trans. Power Electron.*, vol. 34, no. 10, pp. 9655–9670, Oct. 2019.

[12] K. De Brabandere, B. Bolsens, J. Van den Keybus, A. Woyte, J. Driesen, and R. Belmans, "A voltage and frequency droop control method for parallel inverters," *IEEE Trans. Power Electron.* vol. 22, no. 4, pp. 1107–1115, Jul. 2007.

[13] M. C. Chandorkar, D. M. Divan, and R. Adapa, "Control of parallel connected inverters in standalone AC supply systems," *IEEE Trans. Ind. Appl.*, vol. 29, no. 1, pp. 136–143, Jan. 1993.

[14] S. D'Arco and J. A. Suul, "Virtual synchronous machines-classification of implementations and analysis of equivalence to droop controllers for microgrids," in *Proc. IEEE Grenoble Conf.*, Jun. 2013, pp. 1–7.

[15] L. Zhang, L. Harnefors, and H.-P. Nee, "Power-synchronization control of grid-connected voltage-source converters," *IEEE Trans. Power Syst.*, vol. 25, no. 2, pp. 809–820, May 2010.

[16] H. Alrajhi Alsiraji and R. El-Shatshat, "Comprehensive assessment of virtual synchronous machine based voltage source converter controllers," *IET Gener., Transmiss. Distrib.*, vol. 11, no. 7, pp. 1762–1769, May 2017.

[17] M. Ebrahimi, S. A. Khajehoddin, and M. Karimi-Ghartemani, "An improved damping method for virtual synchronous machines," *IEEE Trans. Sustain. Energy*, vol. 10, no. 3, pp. 1491–1500, Jul. 2019.

[18] Q.-C. Zhong, P.-L. Nguyen, Z. Ma, and W. Sheng, "Self-synchronized synchronverters: Inverters without a dedicated synchronization unit," *IEEE Trans. Power Electron.*, vol. 29, no. 2, pp. 617–630, Feb. 2014.

[19] P. Rodriguez, C. Citro, J. I. Candela, J. Rocabert, and A. Luna, "Flexible grid connection and islanding of SPC-based PV power converters," *IEEE Trans. Ind. Appl.*, vol. 54, no. 3, pp. 2690–2702, May 2018.

[20] M. A. Cardiel-Alvarez, J. L. Rodriguez-Amenedo, S. Arnaltes, and M. E. Montilla-DJesus, "Modeling and control of LCC rectifiers for offshore wind farms connected by HVDC links," *IEEE Trans. Energy Convers.*, vol. 32, no. 4, pp. 1284–1296, Dec. 2017.

[21] M. A. Cardiel-Alvarez, S. Arnaltes, J. L. Rodriguez-Amenedo, and A. Nami, "Decentralized control of offshore wind farms connected to diode-based HVdc links," *IEEE Trans. Energy Convers.*, vol. 33, no. 3, pp. 1233–1241, Sep. 2018.

[22] A. Nami, J. L. Rodriguez-Amenedo, S. Arnaltes, M. A. Cardiel-Alvarez, and R. A. Baraciarte, "Frequency control of offshore wind farm with Diode-Rectifier-based HVdc connection," *IEEE Trans. Energy Convers.*, vol. 35, no. 1, pp. 130–138, Mar. 2020.

[23] A. P. Asensio, S. A. Gomez, J. L. Rodriguez-Amenedo, and M. A. Cardiel-Alvarez, "Reactive power synchronization method for voltage-sourced converters," *IEEE Trans. Sustain. Energy*, vol. 10, no. 3, pp. 1430–1438, Jul. 2019.

[24] A. Pena Asensio, S. A. Gomez, J. L. Rodriguez-Amenedo, and M. A. Cardiel-Alvarez, "Decentralized frequency control for black start of full-converter wind turbines," *IEEE Trans. Energy Convers.*, vol. 36, no. 1, pp. 480–487, Mar. 2021.

[25] A. Nami, J. L. R. Amenedo, S. Arnaltes, M. A. C. Alvarez, and R. A. Baraciarte, "Frequency control of offshore wind farms with series-connected diode rectifier units-based HVDC connection," in *Proc. 45th Annu. Conf. IEEE Ind. Electron. Soc. (IECON)*, vol. 1, Oct. 2019, pp. 7057–7062.

[26] A. Nami, J. L. Rodriguez-Amenedo, S. Arnaltes, M. A. C. Alvarez, and R. A. Baraciarte, "Hybrid HVDC system for offshore wind farms connection using series-connected diode rectifier units," in *Proc. 21st Eur. Conf. Power Electron. Appl. (EPE ECCE Europe)*, Sep. 2019, pp. 1–10.

[27] P. Kundur, "Power system stability," in *Power System Stability and Control*. Palo Alto, CA, USA: McGraw-Hill, Electric Power Reseach Institute, 2007, pp. 1–7.

[28] A. Nami, J. L. Rodriguez-Amenedo, S. Arnaltes, M. A. C. Alvarez, and R. A. Baraciarte, "STATCOM operation and control for offshore wind farms with diode rectifier-based HVDC connection," in *Proc. 21st Eur. Conf. Power Electron. Appl. (EPE ECCE Europe)*, Sep. 2019.

[29] W. Wu, N. Pongratananukul, W. Qiu, K. Rustom, T. Kasparis, and I. Batarseh, "DSP-based multiple peak power tracking for expandable power system," in *Proc. 18th Annu. IEEE Appl. Power Electron. Conf. Expo. (APEC)*, vol. 1, Feb. 2003, pp. 525–530.

[30] B. Subudhi and R. Pradhan, "A comparative study on maximum power point tracking techniques for photovoltaic power systems," *IEEE Trans. Sustain. Energy*, vol. 4, no. 1, pp. 89–98, Jan. 2013.

[31] K. H. Hussein, I. Muta, T. Hoshino, and M. Osakada, "Maximum photovoltaic power tracking: An algorithm for rapidly changing atmospheric conditions," *IEE Proc.-Generat., Transmiss. Distrib.*, vol. 142, no. 1, pp. 59–64, Jan. 1995.

[32] X. Sun, W. Wu, X. Li, and Q. Zhao, "A research on photovoltaic energy controlling system with maximum power point tracking," in *Proc. Power Convers. Conf.-Osaka*, vol. 2, 2002, pp. 822–826.

[33] A. Safari and S. Mekhilef, "Simulation and hardware implementation of incremental conductance MPPT with direct control method using cuk converter," *IEEE Trans. Ind. Electron.*, vol. 58, no. 4, pp. 1154–1161, Apr. 2011.

[34] G. J. Kish, J. J. Lee, and P. W. Lehn, "Modelling and control of photovoltaic panels utilising the incremental conductance method for maximum power point tracking," *IET Renew. Power Gener.*, vol. 6, no. 4, pp. 259–266, Jul. 2012.

[35] E. Karatepe and T. Hiyama, "Artificial neural network-polar coordinated fuzzy controller based maximum power point tracking control under partially shaded conditions," *IET Renew. Power Generat.*, vol. 3, no. 2, pp. 239–253, 2009.

[36] A. Yazdani, A. R. Di Fazio, H. Ghoddami, M. Russo, M. Kazerani, J. Jatskevich, K. Strunz, S. Leva, and J. A. Martinez, "Modeling guidelines and a benchmark for power system simulation studies of three-phase single-stage photovoltaic systems," *IEEE Trans. Power Del.*, vol. 26, no. 2, pp. 1247–1264, Apr. 2011.

[37] E. Perez, H. Beltran, N. Aparicio, and P. Rodriguez, "Predictive power control for PV plants with energy storage," *IEEE Trans. Sustain. Energy*, vol. 4, no. 2, pp. 482–490, Apr. 2013.

[38] K. F. Krommydas and A. T. Alexandridis, "Modular control design and stability analysis of isolated PV-source/battery-storage distributed generation systems," *IEEE J. Emerg. Sel. Topics Circuits Syst.*, vol. 5, no. 3, pp. 372–382, Sep. 2015.

[39] J. F. Conroy and R. Watson, "Frequency response capability of full converter wind turbine generators in comparison to conventional generation," *IEEE Trans. Power Syst.*, vol. 23, no. 2, pp. 649–656, May 2008.

[40] Y. Ma, W. Cao, L. Yang, F. F. Wang, and L. M. Tolbert, "Virtual synchronous generator control of full converter wind turbines with short-term energy storage," *IEEE Trans. Ind. Electron.*, vol. 64, no. 11, pp. 8821–8831, Nov. 2017.

[41] A. P. Asensio, S. A. Gómez, J. Rodriguez-Amenedo, M. G. Plaza, J. E.-G. Carrasco, and J. A.-M. de las Morenas, "A voltage and frequency control strategy for stand-alone full converter wind energy conversion systems," *Energies*, vol. 11, no. 3, p. 474, Feb. 2018.

[42] A. Pena Asensio, S. A. Gomez, J. L. Rodriguez-Amenedo, and M. A. Cardiel-Alvarez, "Decentralized frequency control for black start of full-converter wind turbines," *IEEE Trans. Energy Convers.*, vol. 36, no. 1, pp. 480–487, Mar. 2021.

[43] O. Tremblay, L.-A. Dessaint, and A.-I. Dekkiche, "A generic battery model for the dynamic simulation of hybrid electric vehicles," in *Proc. IEEE Vehicle Power Propuls. Conf.*, Sep. 2007, pp. 284–289.
[44] J. Meng, G. Luo, M. Ricco, M. Swierczynski, D.-I. Stroe, and R. Teodorescu, "Overview of lithium-ion battery modeling methods for state-of-charge estimation in electrical vehicles," *Appl. Sci.*, vol. 8, no. 5, p. 659, Apr. 2018.
[45] X. Hu, S. Li, and H. Peng, "A comparative study of equivalent circuit models for li-ion batteries," *J. Power Sources*, vol. 198, pp. 359–367, Jan. 2012.
[46] M. E. Haque, M. Negnevitsky, and K. M. Muttaqi, "A novel control strategy for a variable speed wind turbine with a permanent magnet synchronous generator," in *Proc. IEEE Ind. Appl. Soc. Annu. Meeting*, Oct. 2008, pp. 1–8.
[47] M. Chinchilla, S. Arnaltes, and J. C. Burgos, "Control of permanent-magnet generators applied to variable-speed wind-energy systems connected to the grid," *IEEE Trans. Energy Convers.*, vol. 21, no. 1, pp. 130–135, Mar. 2006.
[48] B. Wu, *Power Conversion and Control of Wind Energy Systems*, vol. 76. Hoboken, NJ, USA: Wiley, 2011.
[49] A. Yazdani and R. Iravani, *Voltage-Sourced Converters in Power Systems*, vol. 39. Hoboken, NJ, USA: Wiley, 2010.
[50] Y. Du, X. Lu, J. Wang, and S. Lukic, "Distributed secondary control strategy for microgrid operation with dynamic boundaries," *IEEE Trans. Smart Grid*, vol. 10, no. 5, pp. 5269–5282, Sep. 2019.
[51] T. L. Vandoorn, B. Meersman, D. Kooning, and L. Vandevelde, "Transition from islanded to grid-connected mode of microgrids with voltage-based droop control," *IEEE Trans. Power Syst.*, vol. 28, no. 3, pp. 2545–2553, Aug. 2013.
[52] S. Lissandron and P. Mattavelli, "A controller for the smooth transition from grid-connected to autonomous operation mode," in *Proc. IEEE Energy Convers. Congr. Expo. (ECCE)*, Sep. 2014, pp. 4298–4305.

JOSÉ LUIS RODRÍGUEZ-AMENEDO (Senior Member, IEEE) received the M.S. degree in industrial engineering from the University Polytechnic of Madrid, in 1994, and the Dr-Ing. (Ph.D.) degree in industrial engineering from the University Carlos III of Madrid, in 2000. From 1999 to 2000, he was with Iberdrola Engineering as a Technology Wind Turbine Manager. From 2001 to 2003, he was with Iberdrola Renewables as a Wind Energy Manager. In 2003, he joined the Department of Electrical Engineering, University Carlos III of Madrid, as an Associate Professor. From 2008 to 2011, he requested an academic leave of absence for founding the technological companies Energy to Quality (E2Q) and Wind to Power Systems (W2PS). His research interests include renewable energy integration into the grid, power electronic converter control, HVDC transmission systems, and energy storage solutions.

SANTIAGO ARNALTES GÓMEZ received the Ph.D. degree in industrial engineering from the Polytechnic University of Madrid, in 1993. He is currently a Full Professor of electrical engineering with the University Carlos III of Madrid. His research interests include modeling, simulation, and control of renewable energy systems and energy storage systems.

JAIME ALONSO-MARTINEZ received the M.Sc. degree in industrial engineering from the Polytechnic University of Madrid, Madrid, Spain, in 2001, and the Ph.D. degree in electrical engineering from the University Carlos III of Madrid, Leganés, Spain, in 2010. He is currently a Visiting Professor with the University Carlos III of Madrid. His research interests include control and optimization of power systems with energy storage and renewable generation.

MARCIAL GONZÁLEZ DE ARMAS received the B.S. degree in electronic engineering and automation from the University of La Laguna, Spain, in 2017, and the M.S. degree in renewable energies and power systems from the University Carlos III of Madrid, Madrid, Spain, in 2018, where he is currently pursuing the Ph.D. degree in electrical engineering. Since 2019, he has been a Research Assistant with the Department of Electrical Engineering, University Carlos III of Madrid. His research interests include control of power converters, grid-forming converters, power system stability, and wind energy conversion systems (WECS).